



# CHORUS

This is the accepted manuscript made available via CHORUS. The article has been published as:

## Updated determination of $N^{\{*\}}$ resonance parameters using a unitary, multichannel formalism

B. C. Hunt and D. M. Manley

Phys. Rev. C **99**, 055205 — Published 20 May 2019

DOI: [10.1103/PhysRevC.99.055205](https://doi.org/10.1103/PhysRevC.99.055205)

# Updated determination of $N^*$ resonance parameters using a unitary, multichannel formalism

B. C. Hunt and D. M. Manley

*Department of Physics, Kent State University, Kent, OH 44242-0001, USA*

(Dated: April 17, 2019)

Results are presented for an updated multichannel energy-dependent partial-wave analysis of  $\pi N$  scattering. Our earlier work incorporated single-energy amplitudes for  $\pi N \rightarrow \pi N$ ,  $\gamma N \rightarrow \pi N$ ,  $\pi N \rightarrow \pi\pi N$ ,  $\pi N \rightarrow \eta N$ , and  $\pi N \rightarrow K\Lambda$ . The present work incorporates new single-energy solutions for  $\gamma p \rightarrow \eta p$  up to a c.m. energy of 1990 MeV,  $\gamma p \rightarrow K^+\Lambda$  up to a c.m. energy of 2230 MeV, and  $\gamma n \rightarrow \eta n$  up to a c.m. energy of 1885 MeV, as well as updated single-energy solutions for  $\pi N \rightarrow \eta N$ ,  $\pi N \rightarrow K\Lambda$ , and  $\gamma N \rightarrow \pi N$ . In this paper, we present and discuss the resonance parameters obtained from a combined fit of all these single-energy amplitudes. Our determined energy-dependent amplitudes provide an excellent description of the corresponding measured observables.

## I. INTRODUCTION

According to quark models, the baryon is typically viewed as a particle composed of three constituent quarks. With sufficient energy, one or more of the quarks can be excited, giving rise to a spectrum of particles called resonances. The primary experimental method used to search for resonances has been to analyze  $\pi N$  reactions including  $\pi N \rightarrow \pi N$  and  $\gamma N \rightarrow \pi N$ . This search has yielded many well-known and established resonances. The first observed resonance, the  $P_{33}(1232)$ , was followed by many others, including the  $S_{11}(1535)$ ,  $S_{11}(1650)$ , and  $F_{15}(1680)$ .

In the literature, there are also many theoretical models [1–5] that attempt to explain the interactions of the quarks inside of baryons. Each of these theoretical models has one thing in common, they predict more resonances than have been experimentally found. One possible explanation is that these predicted resonances decouple from the  $\pi N$  channel. This idea has led to recent experimental efforts using photon beams and meson photoproduction reactions aimed at searching for these resonances.

To aid in the interpretation of the new data, groups such as EBAC-JLab [6], Bonn-Gatchina [7], GWU/SAID [8], and KSU [9] have all developed multichannel formalisms to analyze experimental data in a self-consistent framework. The EBAC-JLab group uses a coupled-channel approach that contains the channels  $\pi N$ ,  $\pi\pi N$ ,  $\eta N$ ,  $K\Lambda$ , and pion photoproduction. Bonn-Gatchina (BnGa) uses a  $K$ -matrix formalism with Breit-Wigner resonances and includes  $\pi N \rightarrow \pi N$ ,  $\gamma N \rightarrow \pi\pi N$ , as well as channels  $\eta N$ ,  $K\Lambda$ , and  $K\Sigma$ . The GWU/SAID model is also based on a  $K$ -matrix approach that focuses on analyses of  $\pi N \rightarrow \pi N$  [10] and  $\gamma N \rightarrow \pi N$  [11], but more recent efforts have allowed the inclusion of  $\pi N \rightarrow \eta N$  as well.

The KSU model [9] used in this work is based on a generalized energy-dependent Breit-Wigner parametrization of amplitudes that treats all channels on an equal footing, and also takes full account of non-resonant backgrounds. Previous fits using this model included partial-wave am-

plitudes for  $\pi N \rightarrow \pi N$ ,  $\pi N \rightarrow \pi\pi N$ ,  $\gamma N \rightarrow \pi N$ ,  $\pi N \rightarrow \eta N$ , and  $\pi N \rightarrow K\Lambda$  [12]. The current work updates and supersedes this earlier work by adding single-energy amplitudes for the photoproduction reactions  $\gamma p \rightarrow \eta p$  and  $\gamma n \rightarrow \eta n$  [13] and  $\gamma p \rightarrow K^+\Lambda$  [14]. Our previous single-energy  $\pi N \rightarrow \eta N$  and  $\pi N \rightarrow K\Lambda$  amplitudes [15] were also updated [16] to be self-consistent with new experimental data for photoproductions reactions having the same final states.

Section II briefly discusses the formalism behind the generalized  $K$ -matrix approach. Section III discusses the fitting procedure used to obtain a fit of the partial-wave amplitudes for each reaction. Section IV discusses results describing the determined resonance structure. Appendix A summarizes details of the KSU Model, which is the parametrization used for our multichannel energy-dependent fits. Appendix B contains tables of partial widths, branching fractions, and resonant amplitudes. It also contains Argand diagrams showing the final dimensionless energy-dependent partial-wave amplitudes.

## II. THEORETICAL MODEL

In the KSU model [9], the unitary and symmetric partial-wave scattering matrix  $\mathbf{S}$ , or  $S$ -matrix, is given by

$$\mathbf{S} = \mathbf{B}^T \mathbf{R} \mathbf{B}, \quad (1)$$

where  $\mathbf{B}^T$  is the transpose of  $\mathbf{B}$ , which is parametrized as a product of unitary, symmetric background matrices

$$\mathbf{B} = \mathbf{B}_1 \mathbf{B}_2 \cdots \mathbf{B}_m \quad (2)$$

and  $\mathbf{R}$  represents the resonant part of the scattering amplitude or  $s$ -channel process. Consequently,  $\mathbf{B}$  itself is unitary but not necessarily symmetric whereas  $\mathbf{S}$  is both unitary and symmetric. This is equivalent to the conservation of probability and time-reversal symmetry. The

matrix  $\mathbf{R}$  is constructed by writing

$$\begin{aligned}\mathbf{R} &= \mathbf{I} + 2i\mathbf{T}_R \\ &= \mathbf{I} + 2i\mathbf{K}(\mathbf{I} - i\mathbf{K})^{-1} \\ &= (\mathbf{I} + i\mathbf{K})(\mathbf{I} - i\mathbf{K})^{-1},\end{aligned}\quad (3)$$

where  $\mathbf{K}$  is a Hermitian  $K$ -matrix,  $\mathbf{K} = \mathbf{K}^\dagger$  and  $\mathbf{I}$  is an identity matrix. To satisfy time-reversal symmetry,  $K$  also must be symmetric.  $\mathbf{T}_R$  is called the resonant transition matrix, or  $T$ -matrix for short. Each of the resonances corresponds to a pole in  $T_R$  and, therefore, also in the total  $S$ -matrix.

In constructing the background, a ‘‘distant poles’’ approximation was used. In this approximation, the functional behavior used for the background was a modified Breit-Wigner form where the mass was kept negative and usually large (the majority have magnitudes greater than 3000 MeV, with many larger than  $10^4$  MeV). This ensured that the background poles exist far from the physical region of the complex plane. The background terms were also allowed very large widths (on the order of  $10^4$  MeV). These features guaranteed that the background had the correct threshold behavior, was slowly varying, and was flexible enough in form to allow the fitting of a large number of potential functional behaviors.

Because scattering can happen off attractive and repulsive potentials, separate background terms were used for each process. An attractive (repulsive) background was assured by using a positive (negative) width for the background, as explained in [17]. In the absence of resonance terms, an attractive (repulsive) background term alone exhibits counter-clockwise (clockwise) motion on an Argand diagram, but such background amplitudes (unlike resonant amplitudes) do not cross the imaginary axis.

All amplitudes used in the parametrization are dimensionless by construction, while the single-energy photoproduction amplitudes [13, 14] have dimensions of mfm. Once an initial single-energy fit has been performed, the dimensioned single-energy amplitudes are converted to dimensionless amplitudes using [17]:

$$\tilde{E}_{l+} = C_I \sqrt{kq(l+1)(l+2)} E_{l+}, \quad (4a)$$

$$\tilde{E}_{(l+1)-} = C_I \sqrt{kql(l+1)} E_{(l+1)-}, \quad (4b)$$

$$\tilde{M}_{l+} = C_I \sqrt{kql(l+1)} M_{l+}, \quad (4c)$$

and

$$\tilde{M}_{(l+1)-} = C_I \sqrt{kq(l+1)(l+2)} M_{(l+1)-}, \quad (4d)$$

where the multipoles with a tilde denote the dimensionless amplitudes. Here  $C_I$  is an isospin coefficient. For  $\gamma N \rightarrow \eta N$  and  $\gamma N \rightarrow K\Lambda$ ,  $C_{1/2} = 1$  and  $C_{3/2} = 0$ . For  $\gamma N \rightarrow \pi N$ ,  $C_{1/2} = -\sqrt{3}$  and  $C_{3/2} = \sqrt{2/3}$ . For

$\gamma N \rightarrow \pi N$ ,  $k$  and  $q$  are the c.m. momentum for the incoming  $\gamma N$  and outgoing  $\pi N$ , respectively, and similarly for  $\gamma N \rightarrow \eta N$  and  $\gamma N \rightarrow K\Lambda$ .

The model contains resonance and background couplings for the reactions  $\pi N \rightarrow \pi N$ ,  $\pi N \rightarrow \pi\pi N$ ,  $\pi N \rightarrow \eta N$ ,  $\pi N \rightarrow K\Lambda$ ,  $\gamma p \rightarrow \eta p$ ,  $\gamma n \rightarrow \eta n$ , and  $\gamma N \rightarrow \pi N$  all of which have single-energy amplitudes determined. It also includes channels that have not been analyzed to date (such as  $\rho\Delta$ ,  $\omega N$ , and  $\pi N^*$ ), which are included in fits as ‘‘dummy channels’’ to satisfy unitarity and prevent over-saturating couplings for measured channels. Further details are presented in Appendix A.

### III. FITTING PROCEDURE

The fitting procedure for obtaining resonance parameters consisted of a two-step process. The first step was to determine single-energy partial-wave amplitudes independent of any resonance structure by fitting observables data in specified energy bins. The single-energy amplitudes for a given partial wave (e.g.,  $S_{11}$  or  $P_{11}$ ) were then fitted as real and imaginary parts with our energy-dependent parametrization to update the resonance parameters and determine corresponding energy-dependent amplitudes. This procedure was iterated until the energy-dependent solution provided a good description of the observables data. The procedure used for fitting was the standard  $\chi^2$  minimization technique.

To gain confidence in both model stability and reaching a global  $\chi^2$  minimum, two techniques were used. The first was to start from a number of distinct solutions and test for convergence in the solution. For this procedure, a local minimum for each starting point was found using the two-step convergence procedure. Each minimum could then be compared to other local minima previously obtained for both a single reaction as well as for all combined reactions. An optimal solution is then one that is sufficiently close to a global minimum for each individual reaction as well as for all reactions combined. The second technique was a randomization process that was devised as follows. A group of resonance parameters were selected to be randomly varied, with each parameter’s random variation independently determined and small. (For instance, the parameters might be all couplings to all  $P_{11}$  resonances.) The random change for the parameters was kept small, usually less than 20% of their starting values. By performing these techniques hundreds of times on different subsets of parameters over the course of the analysis, a large region of parameter space was analyzed and checked. This technique also led to confidence that the determined error bars were reasonable.

To determine final error bars for the single-energy amplitudes, the moduli for each of the partial-wave amplitudes over all newly added photoproduction reactions were treated as free parameters and allowed to vary one final time while the phases were kept fixed in a ‘‘zero-iteration’’ fit. This is described in greater detail in the

papers describing the single-energy analysis [13, 14]. The next step was to put these single-energy amplitudes with their final error bars into the energy-dependent code to generate final error bars for all resonance parameters. In this fit, parameter values were not actually varied and the only purpose of the “fit” was to calculate error bars taking into account all the various correlations between free parameters. The single-energy points that generated a large contribution to  $\chi^2$  had their error bars scaled up until the  $\chi^2$  contribution from those points equaled four. This scaling was done to keep individual points from dominating the results for the fits. Then a full error matrix was calculated with a zero-iteration fit to give the final error bars with all parameters treated as free parameters, but not actually varied. Lastly, the uncertainties in the resonance parameters were scaled by  $\sqrt{\chi^2/\nu}$ , where  $\nu$  was the number of degrees of freedom for the fit.

#### IV. RESULTS

This section is laid out as follows. Section IV A contains information about each of the isospin-1/2 amplitudes and tables of their respective resonance parameters and helicity couplings. Section IV B contains information about the isospin-3/2 amplitudes and tables of their respective resonance parameters and helicity couplings.

##### A. Results for Isospin-1/2 Amplitudes

The following section discusses results for the isospin-1/2 amplitudes. Tables I and II list the Breit-Wigner masses ( $M$ ) and total widths ( $\Gamma(M)$ ) of each isospin-1/2 resonance with errors on the last reported significant figure shown in parentheses. These tables also list pole positions that were calculated numerically with the procedure discussed in Ref. [18] using the actual energy dependence of the Breit-Wigner widths, which is discussed in Appendix A. Only masses are quoted for resonances above 2300 MeV because their widths and couplings are not reliable at this stage of analysis. Tables III and IV show helicity couplings to the isospin-1/2 resonances. Comparisons are made in each table with [19], [20], and [21]. Additional comparisons can be found in the *Review of Particle Physics* (RPP) [22]. Partial widths, branching fractions, and resonant amplitudes ( $\sqrt{xx_i}$ ) are listed in Tables VII and VIII of Appendix B. For a given resonance, the partial widths and quantities directly derived from them (e.g., total widths and branching fractions) in Appendix B were all calculated from energy-dependent partial widths evaluated at the Breit-Wigner mass of the resonance. Finally, the energy-dependent fits for each reaction and resonance are shown in Figs. 1 - 26 of Appendix B.

##### $S_{11}$

This amplitude required four resonances within the fitting region. The first two are the well known  $S_{11}(1535)$  and  $S_{11}(1650)$  and are clearly seen in  $\pi N$ ,  $K\Lambda$ , and  $\eta N$  photoproduction. The properties of the third state,  $S_{11}(1895)$ , especially its mass, were primarily constrained by the  $\pi N \rightarrow \pi N$  and the  $\pi N \rightarrow \eta N$  reactions and it was the  $\pi N \rightarrow \eta N$  reaction that required the resonance. The  $S_{11}(1895)$  was listed as a 2-star resonance in the 2016 edition of the RPP [22], but it was promoted to a 4-star resonance in the 2018 edition [23]. A fourth resonance at 2400 MeV was used to constrain the high-energy behavior of the  $K\Lambda$  channels and remains inconclusive. At this stage of the analysis, its parameters are not reliable and are not quoted.

In general, our parameter values for the  $S_{11}(1535)$  and  $S_{11}(1650)$  are in agreement with results from other works. The primary exception is the  $S_{11}(1535)$  helicity-1/2 coupling found in this work, which is larger than the result by Shrestha *et al.* [12] but is now in agreement with other more recent results. However, results for the  $S_{11}(1895)$  are still not in good agreement between the different groups. For instance, a few groups find a width less than 150 MeV, which is quite narrow, while this and other works find a width in excess of 400 MeV, which is quite large. While the helicity-1/2 couplings show different signs, early indications suggest the resonance has a weak photocoupling. Our fit of the  $S_{11}$  amplitudes contained no dummy channels, meaning that  $S_{11}$  inelasticity can be explained by the measured reactions.

##### $P_{11}$

$P_{11}$  required four resonances, including the well-known Roper resonance  $P_{11}(1440)$ . The Roper resonance shows up in this analysis with a lower mass and width than most current groups seem to find, as well as a larger helicity-1/2 coupling about twice as large. The results for the  $P_{11}(1710)$  are also quite different from other groups because it was never clearly seen in any reaction. In this work it shows up as a clear resonance bump in the reaction  $\gamma p \rightarrow \eta p$  with a well-determined mass and width. Its mass in this work is smaller than that found by other works, while its width is similar to more recent results. Only BnGa finds a large helicity coupling to the resonance (both to the proton and neutron). The agreement between groups for the  $P_{11}(1880)$  resonance is also poor. The  $P_{11}(1880)$  was listed as a 2-star resonance in the 2016 edition of the RPP [22], but it was promoted to a 3-star resonance in the 2018 edition [23]. This work finds a strong helicity-1/2 coupling to the proton for the  $P_{11}(1880)$ , which disagrees with other results. The large resonance coupling was a stable feature of our analysis and was suggested in both the  $\gamma p \rightarrow \eta p$  and  $\gamma p \rightarrow K^+\Lambda$  reactions. Evidence for a strong coupling is strengthened by the fact that even when the amplitude was started

Mass (MeV)	Width (MeV)	Re Pole (MeV)	-2 Im Pole (MeV)	<b>Analysis</b>	Mass (MeV)	Width (MeV)	Re Pole (MeV)	-2 Im Pole (MeV)	<b>Analysis</b>
$S_{11}(1535)$ ****					$S_{11}(1650)$ ****				
1525(2)	147(5)	1496	119	This Work	1666(3)	133(7)	1656	130	This Work
		1499	104	Rönchen 15B			1672	137	Rönchen 15B
1547	188(14)			Workman 12	1635	115(14)			Workman 12
1519(5)	128(14)	1501(4)	134(11)	Anisovich 12	1651(6)	104(10)	1647(6)	103(8)	Anisovich 12
$S_{11}(1895)$ ****					$P_{11}(1440)$ ****				
2000(29)	466(72)	1956	449	This Work	1417(4)	257(11)	1360	186	This Work
-	-	-	-	Rönchen 15B	-	-	1355	215	Rönchen 15B
-	-	-	-	Workman 12	1485(1)	284(4)	-	-	Workman 12
1895(15)	$90^{+30}_{-15}$	1900(15)	$90^{+30}_{-15}$	Anisovich 12	1430(8)	365(35)	1370(4)	190(7)	Anisovich 12
$P_{11}(1710)$ ****					$P_{11}(1880)$ ***				
1648(16)	195(46)	1615	169	This Work	1967(20)	500(77)	1880	429	This Work
-	-	1651	121	Rönchen 15B	-	-	1747	323	Rönchen 15B
-	-	-	-	Workman 12	-	-	-	-	Workman 12
1710(20)	200(18)	1687(17)	200(25)	Anisovich 12	1870(35)	235(65)	1860(35)	250(70)	Anisovich 12
$P_{11}(2100)$ ***					$P_{13}(1720)$ ****				
2221(92)	545(170)	2217	545	This Work	1711(4)	229(22)	1654	100	This Work
-	-	-	-	Rönchen 15B	-	-	1710	219	Rönchen 15B
-	-	-	-	Workman 12	1764	210	-	-	Workman 12
-	-	-	-	Anisovich 12	$1690^{+70}_{-35}$	420(100)	1660(30)	450(100)	Anisovich 12
$P_{13}(1900)$ ****					$P_{13}(2040)$ *				
1911(6)	292(16)	1856	241	This Work	2244(30)	530(89)	2231	529	This Work
-	-	-	-	Rönchen 15B	-	-	-	-	Rönchen 15B
-	-	-	-	Workman 12	-	-	-	-	Workman 12
1905(30)	$250^{+120}_{-50}$	1900(30)	$200^{+100}_{-60}$	Anisovich 12	1525(2)	147(5)	1496	119	Rönchen 15B
$D_{13}(1520)$ ****					$D_{13}(1700)$ ***				
1512.0(1.5)	121(3)	1500	117	This Work	1653(5)	81(13)	1647	79	This Work
-	-	1512	89	Rönchen 15B	-	-	-	-	Rönchen 15B
1515	104	-	-	Workman 12	-	-	-	-	Workman 12
1517(3)	114(5)	1507(3)	111(5)	Anisovich 12	1790(40)	390(140)	1770(40)	420(180)	Anisovich 12
$D_{13}(1875)$ ***					$D_{13}(2120)$ ***				
2005(12)	321(21)	1993	319	This Work	2353(29)	503(62)	2357	503	This Work
-	-	-	-	Rönchen 15B	-	-	-	-	Rönchen 15B
-	-	-	-	Workman 12	-	-	-	-	Workman 12
1880(20)	200(25)	1860(25)	200(20)	Anisovich 12	2150(60)	330(45)	2110(50)	340(45)	Anisovich 12

TABLE I. Comparison of  $S_{11}$ ,  $P_{11}$ ,  $P_{13}$ , and  $D_{13}$  resonance masses, widths, and pole positions for isospin-1/2 amplitudes. The widths listed are the energy-dependent Breit-Wigner total widths evaluated at the resonance masses. Uncertainties in the pole positions should be similar to those in the corresponding Breit-Wigner parameters. Star rating is that found in the RPP [23]. Comparisons are made with works by Rönchen 15b [19], Anisovich 12 [20], and SAID [21].

small and then varied, plots of the modulus showed a distinct bump, which is a signature of a resonance. A fourth  $P_{11}$  resonance at 2200 MeV was included to help explain the high-energy behavior, but nothing conclusive can be said about its properties. This state is listed in

the tables as  $P_{11}(2100)$ . The  $P_{11}(2100)$  was listed as a 1-star resonance in the 2016 edition of the RPP [22], but it was promoted to a 3-star resonance in the 2018 edition [23]. Our fit of the  $P_{11}$  amplitudes used two  $\rho\Delta$  dummy channels.

Mass (MeV)	Width (MeV)	Re Pole (MeV)	-2 Im Pole (MeV)	<b>Analysis</b>	Mass (MeV)	Width (MeV)	Re Pole (MeV)	-2 Im Pole (MeV)	<b>Analysis</b>
$D_{15}(1675)$ ****					$D_{15}(2060)$ ***				
1669(2)	161(8)	1646	146	This Work	2111(17)	499(70)	2010	395	This Work
-	-	1646	125	Rönchen 15B	-	-	-	-	Rönchen 15B
1674(1)	147	-	-	Workman 12	-	-	-	-	Workman 12
1519(5)	128(14)	1501(4)	134(11)	Anisovich 12	2060(15)	375(25)	2040(15)	390(25)	Anisovich 12
$F_{15}(1680)$ ****					$F_{15}(1860)$ **				
1681.0(1)	123(3)	1668	118	This Work	1928(21)	376(58)	1871	337	This Work
-	-	1669	100	Rönchen 15B	-	-	-	-	Rönchen 15B
1680	128	-	-	Workman 12	-	-	-	-	Workman 12
1689(6)	118(6)	1676(6)	113(4)	Anisovich 12	1860 <sup>+120</sup> <sub>-60</sub>	270 <sup>+140</sup> <sub>-50</sub>	1830 <sup>+120</sup> <sub>-60</sub>	250 <sup>+150</sup> <sub>-50</sub>	Anisovich 12
$F_{17}(1990)$ **					$F_{17}(2200)$ new				
2028(19)	490(110)	1913	163	This Work	2219(16)	519(94)	2106	385	This Work
-	-	1738	188	Rönchen 15B	-	-	-	-	Rönchen 15B
-	-	-	-	Workman 12	-	-	-	-	Workman 12
2060(65)	240(50)	2030(65)	240(60)	Anisovich 12	-	-	-	-	Anisovich 12
$G_{17}(2190)$ ****					$G_{19}(2250)$ ****				
2222(15)	442(40)	2162	407	This Work	2200(10)	343(51)	2127	262	This Work
-	-	2074	327	Rönchen 15B	-	-	2062	403	Rönchen 15B
-	-	-	-	Workman 12	-	-	-	-	Workman 12
2180(20)	335(40)	2150(25)	330(30)	Anisovich 12	2280(40)	520(50)	2195(45)	470(50)	Anisovich 12

TABLE II. Comparison of  $D_{15}$ ,  $F_{15}$ ,  $F_{17}$ ,  $G_{17}$ , and  $G_{19}$  resonance masses, widths, and pole positions for isospin-1/2 amplitudes. The widths listed are the energy-dependent Breit-Wigner total widths evaluated at the resonance masses. Uncertainties in the pole positions should be similar to those in the corresponding Breit-Wigner parameters. Star rating is that found in the RPP [22]. Comparisons are made with works by Rönchen 15b [19], Anisovich 12 [20], and SAID [21].

### $P_{13}$

$P_{13}$  required three resonances. It is also the dominant amplitude above the  $S_{11}(1650)$  resonance for the reactions  $\gamma p \rightarrow K^+\Lambda$  and  $\pi^- p \rightarrow K^0\Lambda$ . The mass and width of the  $P_{13}(1720)$  were determined by both  $\gamma p \rightarrow \eta p$  and  $\gamma p \rightarrow K^+\Lambda$ . This is in stark contrast to other analyses that find little or no need for  $P_{13}$  in the reactions involving  $\eta N$ . For the  $P_{13}(1720)$ , the helicity-3/2 coupling to the proton is still in poor agreement between different groups as some works find a small negative value while others (including this work) find a small positive value. Also, BnGa found a large negative helicity-3/2 coupling to the neutron, while other groups (including this work) find a small negative value. The  $P_{13}(1900)$  was first seen in the  $\pi\pi N$  channels [18], but its properties are constrained by  $\gamma p \rightarrow K^+\Lambda$ . The  $P_{13}(1900)$  was listed as a 3-star resonance in the 2016 edition of the RPP [22], but it was promoted to a 4-star resonance in the 2018 edition [23]. Its mass and helicity parameters are now in good agreement between groups, but its width shows disagreement between this work and others such as [12]. A third  $P_{13}$  resonance at 2244 MeV was used to

fit the data above 2000 MeV for the reaction  $\gamma N \rightarrow \pi N$ . The dummy channels for our fit of the  $P_{13}$  amplitudes were  $\rho\Delta$ ,  $\omega N$ , and  $K\Sigma$ .

### $D_{13}$

$D_{13}$  required four resonances. The  $D_{13}(1520)$  is clearly seen in the  $\pi N$  elastic and photoproduction reactions. For this reason, groups generally agree on its parameters. The  $D_{13}(1700)$  resonance was initially seen in  $\pi N \rightarrow \pi\pi N$ , but this work also finds evidence in the reactions  $\gamma p \rightarrow \eta p$  and  $\gamma n \rightarrow \eta n$ . Due to its lack of a strong coupling to a single channel, the resonance has a poorly determined mass and width. The  $D_{13}(1875)$  resonance is hinted at in  $\eta$  photoproduction but with poorly determined properties due to lack of data near 1875 MeV. Its mass in this work is higher than that found in other works except Höhler [24] and its width and helicity couplings are in poor agreement among most groups with a width ranging from 180 to 900 MeV. A fourth  $D_{13}$  resonance at 2353 MeV, listed in the tables as  $D_{13}(2120)$ , was included due to some indication of its existence in the reaction  $\gamma p \rightarrow K^+\Lambda$ . The  $D_{13}(2120)$  was listed as a

$A_{\frac{1}{2}}^p$ (GeV $^{-1/2}$ )	$A_{\frac{1}{2}}^n$ (GeV $^{-1/2}$ )	$A_{\frac{3}{2}}^p$ (GeV $^{-1/2}$ )	$A_{\frac{3}{2}}^n$ (GeV $^{-1/2}$ )	Analysis	$A_{\frac{1}{2}}^p$ (GeV $^{-1/2}$ )	$A_{\frac{1}{2}}^n$ (GeV $^{-1/2}$ )	$A_{\frac{3}{2}}^p$ (GeV $^{-1/2}$ )	$A_{\frac{3}{2}}^n$ (GeV $^{-1/2}$ )	Analysis
$S_{11}(1535)$ ****					$S_{11}(1650)$ ****				
+0.107(3)	-0.055(6)			This Work	+0.048(3)	+0.001(6)			This Work
Not included				Rönchen 15B	Not included				Rönchen 15B
+0.128(4)				Workman 12	+0.055(30)				Workman 12
+0.105(10)	-0.093(11)			Anisovich	+0.033(7)	+0.025(20)			Anisovich
$S_{11}(1895)$ ****					$P_{11}(1440)$ ****				
+0.017(5)	+0.002(13)			This Work	-0.091(7)	+0.013(12)			This Work
-	-	-	-	Rönchen 15B	-	-	-	-	Rönchen 15B
-	-	-	-	Workman 12	-0.056(1)				Workman 12
-0.011(6)	+0.013(6)			Anisovich	-0.061(8)	+0.043(12)			Anisovich
$P_{11}(1710)$ ****					$P_{11}(1880)$ ***				
+0.014(8)	+0.0053(3)			This Work	+0.119(15)	+0.016(10)			This Work
-	-	-	-	Rönchen 15B	-	-	-	-	Rönchen 15B
-	-	-	-	Workman 12	-	-	-	-	Workman 12
+0.052(15)	-0.40(20)			Anisovich	-0.013(3)	+0.034(11)			Anisovich 12a,b
$P_{11}(2100)$ ***					$P_{13}(1720)$ ****				
+0.032(14)	+0.026(13)			This Work	+0.068(4)	-0.064(6)	+0.028(3)	-0.004(6)	This Work
-	-	-	-	Rönchen 15B	-	-	-	-	Rönchen 15B
-	-	-	-	Workman 12	+0.095(2)		-0.048(2)		Workman 12
-	-	-	-	Anisovich 12	+0.110(45)	-0.080(50)	+0.150(30)	-0.140(65)	Anisovich
$P_{13}(1900)$ ****					$P_{13}(2040)$ *				
+0.040(4)	+0.007(14)	-0.094(7)	+0.007(11)	This Work	+0.038(7)	+0.025(21)	+0.078(10)	-0.091(20)	This Work
-	-	-	-	Rönchen 15B	-	-	-	-	Rönchen 15B
-	-	-	-	Workman 12	-	-	-	-	Workman 12
+0.026(15)	+0.000(30)	-0.065(30)	-0.060(45)	Anisovich	-	-	-	-	Anisovich
$D_{13}(1520)$ ****					$D_{13}(1700)$ ***				
-0.034(3)	-0.072(3)	+0.142(3)	-0.123(6)	This Work	+0.032(5)	+0.005(11)	+0.034(6)	-0.094(17)	This Work
-	-	-	-	Rönchen 15B	-	-	-	-	Rönchen 15B
-0.019(2)		+0.141(2)		Workman 12	-	-	-	-	Workman 12
-0.022(4)	-0.049(8)	+0.131(10)	-0.113(12)	Anisovich	+0.041(17)	+0.025(10)	-0.034(13)	-0.032(18)	Anisovich
$D_{13}(1875)$ ***					$D_{13}(2120)$ ***				
-0.013(8)	+0.050(9)	-0.093(9)	+0.141(22)	This Work	+0.047(9)	-0.020(13)	+0.001(7)	-0.00(2)	This Work
-	-	-	-	Rönchen 15B	-	-	-	-	Rönchen 15B
-	-	-	-	Workman 12	-	-	-	-	Workman 12
+0.018(10)	+0.010(6)	-0.009(5)	-0.020(15)	Anisovich		+0.110(45)		+0.040(30)	Anisovich 13b

TABLE III. Comparison of  $S_{11}$ ,  $P_{11}$ ,  $P_{13}$ , and  $D_{13}$  helicity-1/2 and 3/2 amplitudes for both the proton and neutron. Star rating is that found in the RPP [23]. Comparisons are made with works by Rönchen 15b [19], Anisovich 12 [20], and SAID [21].

2-star resonance in the 2016 edition of the RPP [22], but it was promoted to a 3-star resonance in the 2018 edition [23]. No dummy channels were used in our fit of the  $D_{13}$  amplitudes.

$D_{15}$

This partial wave required two resonances, the  $D_{15}(1675)$  and the  $D_{15}(2060)$ . The  $D_{15}(1675)$  has well-defined parameters due to the resonance having a strong coupling to both the  $\pi N$  channel and  $\pi\pi N$  channels. It

$A_{\frac{1}{2}}^p$ (GeV $^{-1/2}$ )	$A_{\frac{1}{2}}^n$ (GeV $^{-1/2}$ )	$A_{\frac{3}{2}}^p$ (GeV $^{-1/2}$ )	$A_{\frac{3}{2}}^n$ (GeV $^{-1/2}$ )	Analysis	$A_{\frac{1}{2}}^p$ (GeV $^{-1/2}$ )	$A_{\frac{1}{2}}^n$ (GeV $^{-1/2}$ )	$A_{\frac{3}{2}}^p$ (GeV $^{-1/2}$ )	$A_{\frac{3}{2}}^n$ (GeV $^{-1/2}$ )	Analysis
$D_{15}(1675)$ ****					$D_{15}(2060)$ ****				
+0.026(2)	-0.069(5)	+0.005(2)	-0.031(5)	This Work	-0.019(5)	+0.069(17)	+0.039(5)	-0.023(20)	This Work
-	-	-	-	Rönchen 15B	-	-	-	-	Rönchen 15B
+0.013(1)	-	+0.016(1)	-	Workman 12	-	-	-	-	Workman 12
+0.024(3)	-0.060(7)	+0.025(7)	-0.088(10)	Anisovich	+0.067(15)	+0.025(11)	+0.055(20)	-0.037(17)	Anisovich
$F_{15}(1680)$ ****					$F_{15}(1860)$ **				
-0.026(4)	+0.005(4)	+0.112(5)	-0.061(4)	This Work	-0.022(20)	+0.021(29)	-0.032(34)	+0.070(35)	This Work
-	-	-	-	Rönchen 15B	-	-	-	-	Rönchen 15B
-0.007(2)	-	+0.140(2)	-	Workman 12	-	-	-	-	Workman 12
-0.013(3)	+0.034(6)	+0.135(6)	+0.044(9)	Anisovich	-0.019(11)	+0.021(13)	+0.048(18)	+0.034(17)	Anisovich
$F_{17}(1990)$ **					$F_{17}(2200)$ new				
+0.006(3)	-0.027(24)	-0.055(8)	+0.051(20)	This Work	-0.000(5)	+0.035(36)	-0.128(13)	+0.031(31)	This Work
-	-	-	-	Rönchen 15B	-	-	-	-	Rönchen 15B
-	-	-	-	Workman 12	-	-	-	-	Workman 12
+0.040(12)	-0.045(20)	+0.057(12)	-0.052(27)	Anisovich	-	-	-	-	Anisovich 12
$G_{17}(2190)$ ****					$G_{19}(2250)$ ****				
+0.001(2)	-0.01(2)	+0.015(3)	-0.023(22)	This Work	+0.0006(37)		+0.013(4)		This Work
-	-	-	-	Rönchen 15B	-	-	-	-	Rönchen 15B
-	-	-	-	Workman 12	-	-	-	-	Workman 12
-0.065(8)	-0.015(13)	+0.035(17)	-0.052(27)	Anisovich	-	-	-	-	Anisovich 12

TABLE IV. Comparison of  $D_{15}$ ,  $F_{15}$ ,  $F_{17}$ ,  $G_{17}$ , and  $G_{19}$  helicity-1/2 and 3/2 amplitudes for both the proton and neutron. Star rating is that found in the RPP [23]. Comparisons are made with works by Rönchen 15b [19], Anisovich 12 [20], and SAID [21].

also contains very little background contributions in most reactions. The main exceptions are the photoproduction reactions on the proton. This is due to the Moorhouse selection rule [25], which states that the first  $D_{15}$  resonance should not couple to  $\gamma p$ . The  $D_{15}(2060)$  is seen in the data for the reaction  $\gamma p \rightarrow K^+\Lambda$  and was necessary to obtain a good fit to differential cross-section data above 2000 MeV. The  $D_{15}(2060)$  was listed as a 2-star resonance in the 2016 edition of the RPP [22], but it was promoted to a 3-star resonance in the 2018 edition [23]. The only dummy channel for our fit of the  $D_{15}$  amplitudes was a  $\rho\Delta$  channel.

### $F_{15}$

$F_{15}$  needed three resonances, including the  $F_{15}(1680)$  and  $F_{15}(1860)$ . The  $F_{15}(1680)$  is well determined from pion reactions and groups agree on its parameters. The  $F_{15}(1860)$  is less clear but necessary to fit the high-energy behavior of  $\eta$  photoproduction. There is also a hint of a resonance in  $\pi N \rightarrow \pi N$  where a small bump does appear. However, a good fit of the bump proved difficult as improvements in the fit to the imaginary part degraded fits to the real part. This may be one reason groups tend

to agree on its mass but not its width. A third resonance at 2320 MeV was clear in the magnetic amplitude for the reaction  $\gamma p \rightarrow K^+\Lambda$ . No dummy channels were used in our fit of the  $F_{15}$  amplitudes.

### $F_{17}$

$F_{17}$  needed two resonances, namely the  $F_{17}(1990)$  and  $F_{17}(2200)$ . The  $F_{17}(1990)$  has poorly determined parameters and was not conclusively seen in any reaction, although there are hints that it is necessary in  $\gamma p \rightarrow \eta p$ ,  $\gamma p \rightarrow K^+\Lambda$ , and perhaps  $\pi N \rightarrow \pi N$ . The  $F_{17}(2200)$  is a new state that was added to fit the indication of a higher-lying resonance in  $\pi N \rightarrow \pi N$  where the imaginary part starts increasing above 2000 MeV. Based on the single-energy solution, it appears it will peak just above 2300 MeV. This work also finds the  $F_{17}(2200)$  has a strong coupling to  $K\Lambda$ . This is in agreement with quark-model predictions from [26]. A reliable determination of its parameters would most likely require data up to 2400 MeV in a number of reactions, including  $\pi N \rightarrow \pi N$ . This amplitude was also critical for describing the forward-angle shape of the differential cross section at energies above 1800 MeV for the reaction



$\pi^- p \rightarrow \eta n$ . The dummy channels in our fit of the  $F_{17}$  amplitudes were  $K\Sigma$ ,  $\omega N$ , and  $\rho\Delta$ .

### $G_{17}$ and $G_{19}$

The  $G_{17}(2190)$  and  $G_{19}(2250)$  resonances were used in the higher amplitudes and are seen primarily in  $\pi N \rightarrow \pi N$ . Both resonances had negligible helicity coupling and are not seen in any photoproduction reaction. Groups generally agree on the resonance parameters for  $G_{17}(2190)$  because it clearly appears in  $\pi N \rightarrow \pi N$ ; however, the properties of  $G_{19}(2250)$  show significant disagreement between groups. The only agreement is that its mass is most likely above 2200 MeV. An  $\omega N$  dummy channel was used in our fit of the  $G_{17}$  amplitudes while a  $\rho N$  dummy channel was used in our fit of the  $G_{19}$  amplitudes.

## B. Results for Isospin-3/2 Amplitudes

The following section discusses results for the isospin-3/2 amplitudes. Table V lists the Breit-Wigner masses ( $M$ ) and total widths ( $\Gamma(M)$ ) for each isospin-3/2 resonance with uncertainties on the last reported significant figure shown in parentheses. The tables also list pole positions that were calculated numerically with the procedure discussed in Ref. [18] using the actual energy dependence of the Breit-Wigner widths, which is discussed in Appendix A. Table VI shows helicity-3/2 couplings for each resonance. Table IX of Appendix B shows the partial widths ( $\Gamma_i$ ), branching fractions ( $\mathcal{B}_i$ ), and resonant amplitudes ( $\sqrt{x x_i}$ ) for each amplitude's included channels. For a given resonance, the partial widths and quantities directly derived from them (e.g., total widths and branching fractions) in Appendix B were all calculated from energy-dependent partial widths evaluated at the Breit-Wigner mass of the resonance.

### $S_{31}$

For this partial wave, two resonances were used. Our results for the  $S_{31}(1620)$  are in good agreement with those of other groups despite the large repulsive background that appears at low energies in the  $\pi N \rightarrow \pi N$  amplitude, which could potentially distort its properties. The  $S_{31}(1900)$  was listed as a 2-star resonance in the 2016 edition of the RPP [22], but it was promoted to a 3-star resonance in the 2018 edition [23]. The  $S_{31}(1900)$  mass and width found in this work are significantly larger than values found by other groups. The helicity couplings found in this work for both resonances now agree with other recent results except Shrestha *et al.* [12]. One surprise in the results from this work is the strength of the  $S_{31}(1900)$  helicity-1/2 coupling. While the size of the coupling is large, there is no significant indication in the

single-energy solution for pion photoproduction that it should be significantly smaller and an overall coupling was important to fit the differential cross-section data in the reaction  $\gamma N \rightarrow \pi N$ , which other groups are unable to fit [16]. No dummy channels were needed to fit the  $S_{31}$  amplitudes.

### $P_{31}$

$P_{31}$  needed two resonances, the  $P_{31}(1910)$  and a new high-mass state. This partial wave shows significant repulsive background in the  $\pi N \rightarrow \pi N$  amplitude. The mass of the  $P_{31}(1910)$  resonance was lower than that found by other recent analyses but in agreement with results by older analyses. One concern with this amplitude is the size of the helicity-1/2 coupling. The single-energy solution suggests that perhaps the overall coupling is too large, but the existence of a few points above the energy-dependent fit that also have smaller error bars makes it difficult to obtain any definitive conclusion. The  $\pi N$  coupling to the resonance is in very good agreement with results by other groups [22], which implies that there is no obvious reason to increase its value while decreasing the helicity coupling. A new resonance,  $P_{31}(2250)$ , was used to fit the  $\pi N \rightarrow \pi N$  amplitude at energies above 2000 MeV and was also used to fit the real part of the pion photoproduction amplitude. A  $\rho\Delta$  dummy channel was used for our fit of the  $P_{31}$  amplitudes.

### $P_{33}$

$P_{33}$  needed three resonances, including the  $P_{33}(1232)$  and the  $P_{33}(1600)$ . Our results for the  $P_{33}(1232)$  are in good agreement with other groups, which is to be expected due to its dominance in the elastic and pion photoproduction reactions. The  $P_{31}(1600)$  was listed as a 3-star resonance in the 2016 edition of the RPP [22], but it was promoted to a 4-star resonance in the 2018 edition [23]. The  $P_{33}(1600)$  was needed for the  $\pi\pi N$  reactions and various groups disagree about its properties. A few groups such as BnGa and Höhler [24] find masses near 1510 MeV, while other works, including this one, find a mass above 1600 MeV. The positive helicity couplings found in this work agree with results by Shrestha [12] in sign and magnitude, while other groups find negative values. A third resonance at 2250 MeV has parameter values that differ significantly between groups, which shows that its properties are still poorly determined. Figure 22 in Appendix B for the  $\pi N$  elastic channel shows that the reaction saturates the unitary bound nearly up to 1500 MeV where  $\pi\pi N$  channels become important. We included  $\rho\Delta$  and  $K\Sigma$  as dummy channels for our fit of the  $P_{33}$  amplitudes.

Mass (MeV)	Width (MeV)	Pole (Re)	Pole (-2Im)	Analysis	Mass (MeV)	Width (MeV)	Pole (MeV)	Pole (MeV)	Analysis
$S_{31}(1620)$ ****					$S_{31}(1900)$ ***				
1589(3)	107(7)	1577	101	This Work	1989(22)	457(60)	1957	447	This Work
		1600	65	Rönchen 15B	–	–	–	–	Rönchen 15B
1615	147			Workman 12	–	–	–	–	Workman 12
1600(8)	130(11)	1597(4)	130(9)	Anisovich 12	1840(30)	300(45)	1845(25)	300(45)	Anisovich 12
$P_{31}(1910)$ ****					$P_{31}(2250)$ <b>new</b>				
1846(18)	260(57)	1801	224	This Work	2250(30)	320(120)	2250	320	This Work
		1799	648	Rönchen 15B	–	–	–	–	Rönchen 15B
–	–	–	–	Workman 12	–	–	–	–	Workman 12
1860(40)	350(55)	1850(40)	350(45)	Anisovich 12	–	–	–	–	Anisovich 12
$P_{33}(1232)$ ****					$P_{33}(1600)$ ****				
1230.8(4)	110.9(8)	1212.4	96.8	This Work	1664(16)	322(46)	1619	295	This Work
–	–	1218	92	Rönchen 15B	–	–	1552	350	Rönchen 15B
1233	119	–	–	Workman 12	–	–	–	–	Workman 12
1228(2)	110(3)	1210.5(10)	99(2)	Anisovich 12	1510(20)	220(45)	1498(25)	230(50)	Anisovich 12
$P_{33}(1920)$ ***					$D_{33}(1700)$ ****				
1976.0(49)	509(170)	1910	472	This Work	1720(5)	226(14)	1693	213	This Work
–	–	1715	882	Rönchen 15B	–	–	1677	305	Rönchen 15B
–	–	–	–	Workman 12	1695	376	–	–	Workman 12
1900(30)	310(60)	1890(30)	300(60)	Anisovich 12	1715 <sup>+30</sup> <sub>-15</sub>	310 <sup>+40</sup> <sub>-15</sub>	1680(10)	305(15)	Anisovich 12
$D_{33}(1940)$ **					$D_{35}(1930)$ ***				
2137(13)	400(43)	2139	400	This Work	1988(32)	500(160)	1863	260	This Work
–	–	–	–	Rönchen 15B	–	–	1836	724	Rönchen 15B
–	–	–	–	Workman 12	–	–	–	–	Workman 12
1995 <sup>+105</sup> <sub>-60</sub>	450(100)	1990 <sup>+100</sup> <sub>-50</sub>	450(90)	Anisovich 12	–	–	–	–	Anisovich 12
$F_{35}(1905)$ ****					$F_{37}(1950)$ ****				
1866(9)	289(20)	1819	253	This Work	1913(4)	241(10)	1871	206	This Work
–	–	1795	247	Rönchen 15B	–	–	–	–	Rönchen 15B
1858	321	–	–	Workman 12	–	–	–	–	Workman 12
1861(6)	335(18)	1805(10)	300(15)	Anisovich 12	1915(6)	246(10)	1890(4)	243(8)	Anisovich 12

TABLE V. Comparison of resonance masses, widths, and pole positions for isospin-3/2 amplitudes. The widths listed are the energy-dependent Breit-Wigner total widths evaluated at the resonance masses. Uncertainties in the pole positions should be similar to those in the corresponding Breit-Wigner parameters.

### $D_{33}$

$D_{33}$  needed two resonances. The  $D_{33}(1700)$  is well known and our values for its mass and width agree well with prior analyses. In addition, our value for its helicity-1/2 coupling is in agreement with more recent results. This work found a second  $D_{33}$  resonance at 2137 MeV. Its parameters in general differ from those of other works, and some groups, including SAID [11], do not include a second resonance in their fits, despite this work having found significant evidence for its existence in  $\gamma N \rightarrow \pi N$ . Interestingly, the helicity-1/2 coupling found in this work

agrees with the work by Sokhoyan [27], but the helicity-3/2 coupling differs in sign. No dummy channels were needed for our fit of the  $D_{33}$  amplitudes.

### $D_{35}$

This partial wave needed only the  $D_{35}(1930)$  resonance. Its mass is similar to that found by other works except Arndt [10], while its width varies significantly among the different analyses. The helicity couplings also show differing signs and strengths among the different

analyses. This work found a significant negative helicity-1/2 coupling to the resonance, while other groups have found a small coupling. A  $\rho\Delta$  dummy channel was used for our fit of the  $D_{35}$  amplitudes.

### $F_{35}$

This partial wave needed the  $F_{35}(1905)$  resonance and a higher-mass state. The mass, width, and helicity couplings of  $F_{35}(1905)$  are in good agreement among the different analyses, in part, because there is a clear indication for its existence in  $\pi N \rightarrow \pi N$ . A second  $F_{35}$  state was needed at 2340 MeV to fit the high-energy behavior of the  $\pi N \rightarrow \pi N$  amplitude and the suggestion of a structure appearing in pion photoproduction. No dummy channels were needed in our fit of the  $F_{35}$  amplitudes.

### $F_{37}$

$F_{37}$  needed two resonances, the  $F_{37}(1950)$  and  $F_{37}(2390)$ . The  $F_{37}(1950)$  has mass, width, and helicity couplings that are in good agreement among the different analyses and clearly appears in the  $\pi N \rightarrow \pi N$  amplitude. The second resonance is located at 2390 MeV and was used to constrain the amplitudes at high energies, but there currently is only weak evidence for its existence. This state is listed as a 1-star resonance in the 2018 edition of the RPP [23]. We included  $\rho\Delta$  and  $K\Sigma$  as dummy channels in our fit of the  $F_{37}$  amplitudes.

### $G_{37}$ and $G_{39}$

Our fits of the  $G_{37}$  and  $G_{39}$  amplitudes included only a single resonance with masses of 2330 MeV and 2300 MeV, respectively. Due to their high masses, their individual parameters are poorly determined and are not quoted.

## V. SUMMARY AND CONCLUSIONS

An updated multichannel, partial-wave analysis was performed by including newly determined single-energy amplitudes for the reactions  $\gamma p \rightarrow \eta p$ ,  $\gamma p \rightarrow K^+\Lambda$ , and  $\gamma n \rightarrow \eta n$  in our energy-dependent fits of the various partial waves. The proton helicity coupling to the  $S_{11}(1535)$  is now in agreement with results from other works. Also, a new  $F_{17}$  resonance near 2200 MeV was needed to fit the  $\pi N \rightarrow \pi N$ ,  $\gamma N \rightarrow \pi N$ , and  $\gamma p \rightarrow K^+\Lambda$  reactions. This is consistent with quark-model predictions from [5] that an  $F_{17}$  resonance couples to  $K\Lambda$ . Additional data at energies above 2200 MeV are needed to both confirm its existence and determine its properties. In addition to our updated determination of resonance parameters, our fits yield a new energy-dependent solution for all the various partial-wave and multipole amplitudes. This energy-dependent solution provides an excellent description [13, 14] of the observables data used to determine the final single-energy amplitudes.

## ACKNOWLEDGMENTS

The authors would like to thank Dr. Igor Strakovsky for supplying much of the photoproduction database used for our single-energy analyses. This work was supported in part by the U.S. Department of Energy, Office of Science, Office of Nuclear Physics Research Division, under Awards No. DE-FG02-01ER41194 and DE-SC0014323, and by the Department of Physics at Kent State University.

- 
- [1] N. Isgur and G. Karl, Phys. Rev. D **19**, 2653 (1979); erratum: Phys. Rev. D **23**, 817 (1981).
  - [2] S. Capstick and N. Isgur, Phys. Rev. D **34**, 2809 (1986).
  - [3] L. Y. Glozman, W. Plessas, K. Varga, and R. F. Wagenbrunn, Phys. Rev. D **58**, 094030 (1998).
  - [4] U. Löring, B. Ch. Metsch, and H. R. Petry, Euro. Phys. J. A **10**, 395 (2001).
  - [5] S. Capstick and W. Roberts, Prog. Part. Nucl. Phys. **45**, S241 (2000).
  - [6] B. Julia-Diaz, T. S. H. Lee, A. Matsuyama, and T. Sato, Phys. Rev. C **76**, 065201 (2007).
  - [7] A. Sarantsev, Chinese Phys. C **33**, 1085 (2009).
  - [8] R. A. Arndt, W. J. Briscoe, I. I. Strakovsky, and R. L. Workman, Phys. Rev. C **74**, 045205 (2006).
  - [9] D. M. Manley, Few-Body Systems Suppl. **11**, 104 (1999); D. M. Manley, Int. J. Mod. Phys. A **18**, 441 (2003).
  - [10] R. A. Arndt, W. J. Briscoe, I. I. Strakovsky, and R. L. Workman, Phys. Rev. C **74**, 045205 (2006).
  - [11] P. Adlarson *et al.*, Phys. Rev. C **92**, 24617 (2015).
  - [12] M. Shrestha and D. M. Manley, Phys. Rev. C **86**, 055203 (2012).
  - [13] B. C. Hunt and D. M. Manley, arXiv:1804.06031 [nucl.ex] (submitted to Phys. Rev. C).
  - [14] B. C. Hunt and D. M. Manley, arXiv:1804.07422 [nucl.ex] (submitted to Phys. Rev. C).
  - [15] M. Shrestha and D. M. Manley, Phys. Rev. C **86**, 045204 (2012).
  - [16] B. C. Hunt, Ph.D. dissertation, Kent State University (2017).

$A_{\frac{1}{2}}^N$ (GeV $^{-1/2}$ )	$A_{\frac{3}{2}}^N$ (GeV $^{-1/2}$ )	Analysis	$A_{\frac{1}{2}}^N$ (GeV $^{-1/2}$ )	$A_{\frac{3}{2}}^N$ (GeV $^{-1/2}$ )	Analysis
$S_{31}(1620)$ ****			$S_{31}(1900)$ ***		
+0.0124(7)	–	This Work	+0.212(29)	–	This Work
–	–	Rönchen 15B	–	–	Rönchen 15B
+0.029(3)	–	Workman 12	–	–	Workman 12
+0.052(5)	–	Anisovich 12	+0.059(16)	–	Anisovich 12
$P_{31}(1910)$ ****			$P_{31}(2250)$ new		
+0.203(56)	–	This Work	–0.054(28)	–	This Work
–	–	Rönchen 15B	–	–	Rönchen 15B
–	–	Workman 12	–	–	Workman 12
+0.022(9)	–	Anisovich 12	–	–	Anisovich 12
$P_{33}(1232)$ ****			$P_{33}(1600)$ ****		
–0.146(2)	–0.250(2)	This Work	+0.0082(14)	+0.048(14)	This Work
–	–	Rönchen 15B	–	–	Rönchen 15B
–0.139(2)	–0.262(3)	Workman 12	–	–	Workman 12
–0.131(4)	–0.254(5)	Anisovich 12	–0.050(9)	–0.040(12)	Anisovich 12
$P_{33}(1920)$ ***			$D_{33}(1700)$ ****		
–0.028(10)	–0.043(14)	This Work	+0.156(17)	+0.0125(16)	This Work
–	–	Rönchen 15B	–	–	Rönchen 15B
–	–	Workman 12	+0.105(5)	+0.092(4)	Workman 12
+0.130 $^{+30}_{-60}$	–0.115 $^{+25}_{-50}$	Anisovich 12	+0.160(20)	+0.165(25)	Anisovich 12
$D_{33}(1940)$ **			$D_{35}(1930)$ ***		
+0.1614(31)	–0.209(23)	This Work	–0.043(8)	–0.020(17)	This Work
–	–	Rönchen 15B	–	–	Rönchen 15B
–	–	Workman 12	–	–	Workman 12
–	–	Anisovich 12	–	–	Anisovich 12
$F_{35}(1905)$ ****			$F_{37}(1950)$ ****		
+0.077(10)	–0.053(29)	This Work	–0.047(2)	–0.074(2)	This Work
–	–	Rönchen 15B	–	–	Rönchen 15B
+0.019(2)	–0.038(4)	Workman 12	–0.083(4)	–0.096(4)	Workman 12
+0.025(5)	–0.049(4)	Anisovich 12	–0.071(4)	–0.094(5)	Anisovich 12

TABLE VI. Comparison of  $S_{31}$ ,  $P_{31}$ ,  $P_{33}$ ,  $D_{33}$ ,  $D_{35}$ ,  $F_{35}$ , and  $F_{37}$  helicity-1/2 and 3/2 amplitudes for both the proton and neutron. Star rating is that found in the RPP [22]. Comparisons are made with works by Rönchen 15b [19], Anisovich 12 [20], and SAID [21]

- [17] M. M. Niboh, Ph.D. dissertation, Kent State University (1997).
- [18] D. M. Manley, Phys. Rev. D **51**, 4837 (1995).
- [19] D. Rönchen *et al.*, Euro. Phys. J. A **51**, 70 (2015).
- [20] A. V. Anisovich *et al.*, Euro. Phys. J. A **48**, 15 (2012).
- [21] R. Workman, M. W. Paris, W. J. Briscoe, I. I. Strakovsky, Phys. Rev. C **86**, 15202 (2012).
- [22] C. Patrignani *et al.* (Particle Data Group), Chin. Phys. C **40**, 100001 (2016).
- [23] M. Tanabashi *et al.* (Particle Data Group), Phys. Rev. D **98**, 030001 (2018).
- [24] G. Höhler *et al.*, Physik Daten 12-1 (1979).
- [25] R. G. Moorhouse, Phys. Rev. Lett. **16**, 772 (1966).
- [26] S. Capstick and W. Roberts, Phys. Rev. D **58**, 074011 (1998).
- [27] V. Sokhoyan *et al.*, Euro. Phys. J. A **51**, 95 (2015).
- [28] Hongyu Zhang, Ph.D. dissertation, Kent State University (2008).
- [29] J. M. Blatt and V. F. Weisskopf, *Theoretical Nuclear Physics* (Wiley, 1966).
- [30] See supplemental material at [url provided by PRC] for a data file containing the single-energy amplitudes shown in the Argand diagrams.

## Appendix A: KSU Model

As noted in Sec. II, the KSU model parametrizes the partial-wave  $S$ -matrix by

$$\mathbf{S} = \mathbf{B}^T \mathbf{R} \mathbf{B}, \quad (\text{A1})$$

where  $\mathbf{R}$  represents the resonant part of the  $S$ -matrix and  $\mathbf{B}$  represents background contributions. The matrix  $\mathbf{R}$  is a phenomenological representation of scattering contributions from  $s$ -channel exchange processes while  $\mathbf{B}$  is a phenomenological representation of contributions from  $t$ - and  $u$ -channel exchange processes. The matrix  $\mathbf{R}$  is constructed by writing

$$\mathbf{R} = \mathbf{I} + 2i\mathbf{T}_R = (\mathbf{I} + i\mathbf{K})(\mathbf{I} - i\mathbf{K})^{-1}, \quad (\text{A2})$$

where  $\mathbf{K}$  is a symmetric Hermitian  $K$ -matrix,  $\mathbf{K} = \mathbf{K}^\dagger$ . It follows that the resonant  $T$ -matrix is

$$\mathbf{T}_R = \mathbf{K} + i\mathbf{T}_R \mathbf{K}, \quad (\text{A3})$$

so that the matrix elements are related by

$$\mathbf{T}_{Rij} = \mathbf{K}_{ij} + i \sum_{k=1}^n \mathbf{T}_{Rik} \mathbf{K}_{kj}, \quad (\text{A4})$$

where  $n$  is the number of reaction channels.

It is convenient to introduce functions  $T_\alpha$  defined as

$$T_\alpha = \sin \Theta_\alpha e^{i\Theta_\alpha} = \frac{\tan \Theta_\alpha}{1 - i \tan \Theta_\alpha}, \quad (\text{A5})$$

where we write

$$\tan \Theta_\alpha = \frac{\gamma_\alpha}{M_\alpha - W}, \quad (\text{A6})$$

where  $W$  is the total c.m. energy and  $M_\alpha$  and  $\gamma_\alpha$  are functions of  $W$ . In the KSU model, we use the parametrization

$$\mathbf{K}_{ij} = \sum_{\alpha=1}^N \tan \Theta_\alpha x_i^\alpha x_j^\alpha, \quad (\text{A7})$$

where  $N$  is the number of resonances in the energy range of the fit. The energy dependence of  $\Theta_\alpha$  is determined in a nontrivial way to facilitate the determination of pole positions in the corresponding  $\mathbf{R}$  matrix. Each resonance corresponds to a simple pole in  $\mathbf{R}$  and, therefore, also in the full  $S$ -matrix. The factors  $x_i^\alpha$  are constructed to satisfy the condition

$$\sum_{i=1}^n (x_i^\alpha)^2 = 1. \quad (\text{A8})$$

We also define

$$\epsilon_{\alpha\beta} = \epsilon_{\beta\alpha} = \sum_{i=1}^n x_i^\alpha x_i^\beta. \quad (\text{A9})$$

If we drop the resonance superscript ( $\alpha$ ), we identify  $x_i = \epsilon_i \sqrt{\Gamma_i / \Gamma_{\text{total}}}$ , where  $\Gamma_i$  is the energy-dependent partial width for the resonance to decay into the  $i$ -th channel,  $\Gamma_{\text{total}} = \sum_{i=1}^n \Gamma_i$  is the energy-dependent total width, and  $\epsilon_i = \pm 1$  is the sign of the coupling of the resonance to the  $i$ -th channel. By using these properties, it is possible to determine an explicit expression for  $\mathbf{T}_{Rij}$  in terms of the functions  $\tan \Theta_\alpha$  and the  $x_i^\alpha$ .

### 1. One-Resonance Case

For the simple case of a single resonance, the matrix  $\mathbf{T}_R$  has elements

$$\mathbf{T}_{Rij} = T_1 x_i^1 x_j^1 = \frac{\gamma_1}{M_1 - W - i\gamma_1} x_i^1 x_j^1, \quad (\text{A10})$$

where here,  $M_1$  is identified as the Breit-Wigner mass parameter and  $\gamma_1 = \Gamma_1/2$ , where  $\Gamma_1$  is the Breit-Wigner energy-dependent total width of the resonance.

### 2. Two-Resonance Case

For the case of two resonances, the matrix  $\mathbf{T}_R$  has elements

$$\mathbf{T}_{Rij} = \mathcal{D}_2^{-1} [T_1 x_i^1 x_j^1 + T_2 x_i^2 x_j^2 + i\epsilon_{12} T_1 T_2 (x_i^1 x_j^2 + x_i^2 x_j^1)], \quad (\text{A11})$$

where  $\mathcal{D}_2 = 1 + \epsilon_{12}^2 T_1 T_2$ . The poles of  $\mathbf{T}_R$  occur at complex energies where  $\mathcal{D}_2 = 0$ . When this equation is written in terms of the set of functions  $(M_1, M_2; \gamma_1, \gamma_2)$ , a quadratic equation in  $W$  results. This equation may be rewritten in factorized form as  $(W - W_a)(W - W_b) = 0$ , where  $W_a = M_a - i\gamma_a$  and  $W_b = M_b - i\gamma_b$  with the Breit-Wigner parameters being the set  $(M_a, M_b; \Gamma_a, \Gamma_b)$ , where  $\gamma_a = \Gamma_a/2$  and  $\gamma_b = \Gamma_b/2$ . The relationship between the energy-dependent  $\mathbf{K}$ -matrix parameters  $(M_1, M_2; \gamma_1, \gamma_2)$  and the Breit-Wigner  $\mathbf{T}_R$ -matrix parameters  $(M_a, M_b; \gamma_a, \gamma_b)$  is given by the following set of coupled equations:

$$\begin{aligned} M_1 + M_2 &= M_a + M_b, \\ \gamma_1 + \gamma_2 &= \gamma_a + \gamma_b, \\ M_1 \gamma_2 + M_2 \gamma_1 &= M_a \gamma_b + M_b \gamma_a, \\ M_1 M_2 - (1 - \epsilon_{12}^2) \gamma_1 \gamma_2 &= M_a M_b - \gamma_a \gamma_b. \end{aligned} \quad (\text{A12})$$

When  $\epsilon_{ij}^2 = \epsilon_{ji}^2 \ll 1$  ( $i \neq j$ ), it is possible to reach the approximate analytic solution:

$$\begin{aligned} M_1 &\approx M_a + \frac{\epsilon_{12}^2 \gamma_a \gamma_b}{(M_a - M_b)^2 + (\gamma_a - \gamma_b)^2} (M_a - M_b), \\ M_2 &\approx M_b + \frac{\epsilon_{21}^2 \gamma_b \gamma_a}{(M_b - M_a)^2 + (\gamma_b - \gamma_a)^2} (M_b - M_a), \\ \gamma_1 &\approx \gamma_a - \frac{\epsilon_{12}^2 \gamma_a \gamma_b}{(M_a - M_b)^2 + (\gamma_a - \gamma_b)^2} (\gamma_a - \gamma_b), \\ \gamma_2 &\approx \gamma_b - \frac{\epsilon_{21}^2 \gamma_b \gamma_a}{(M_b - M_a)^2 + (\gamma_b - \gamma_a)^2} (\gamma_b - \gamma_a). \end{aligned} \quad (\text{A13})$$

### 3. Arbitrary Number of Resonances

A detailed discussion of the cases for three and four resonances can be found in Ref. [28]. For an arbitrary number  $N$  of resonances, the relationship between the energy-dependent  $\mathbf{K}$ -matrix parameters  $(M_1, M_2, \dots; \gamma_1, \gamma_2, \dots)$  and the Breit-Wigner  $\mathbf{T}_{\mathbf{R}}$ -matrix parameters  $(M_{a_1}, M_{a_2}, \dots; \gamma_{a_1}, \gamma_{a_2}, \dots)$  is approximately given by

$$\begin{aligned} M_i &\approx M_{a_i} + \sum_{j \neq i}^N \frac{\epsilon_{ij}^2 \gamma_{a_i} \gamma_{a_j}}{(M_{a_i} - M_{a_j})^2 + (\gamma_{a_i} - \gamma_{a_j})^2} (M_{a_i} - M_{a_j}), \\ \gamma_i &\approx \gamma_{a_i} - \sum_{j \neq i}^N \frac{\epsilon_{ij}^2 \gamma_{a_i} \gamma_{a_j}}{(M_{a_i} - M_{a_j})^2 + (\gamma_{a_i} - \gamma_{a_j})^2} (\gamma_{a_i} - \gamma_{a_j}), \end{aligned} \quad (\text{A14})$$

for  $i = 1, \dots, N$ . We have determined that this approximation gives excellent agreement with a direct numerical solution of the coupled nonlinear equations that relate the  $\mathbf{K}$ -matrix parameters and the  $\mathbf{T}_{\mathbf{R}}$ -matrix parameters.

### 4. Parametrization of Energy-Dependent Partial Widths

In the KSU model, the energy-dependent Breit-Wigner partial width for the  $r$ -th resonance to decay into the  $i$ -th channel was parametrized as  $\Gamma_{ir}(W) = \lambda_r \delta_i(W)$ , where  $\lambda_r$  is a constant and  $\delta_i(W)$  is a phase-space factor that is defined below. If  $M_r$  is the Breit-Wigner mass (a fitting parameter) of the resonance and if  $\delta_i(M_r) \neq 0$ , then the partial width of the  $r$ -th resonance to decay into the  $i$ -th channel can be rewritten as

$$\Gamma_{ir}(W) = \Gamma_{ir}(M_r) \frac{\delta_i(W)}{\delta_i(M_r)}, \quad (\text{A15})$$

where  $\Gamma_{ir}(M_r)$  is the partial width for the decay of the  $r$ -th resonance into the  $i$ -th channel, evaluated at  $W = M_r$ . The actual fitting parameters are the Breit-Wigner masses  $M_r$  and the signed couplings  $\sqrt{\Gamma_{ir}(M_r)}$ ,

where signs were determined relative to the  $\pi N$  channel. Our fitted values of the Breit-Wigner masses  $M_r$  and the partial widths  $\Gamma_{ir}(M_r)$  are tabulated in Appendix B.

For the two-body decay of a resonance into an  $i$ -th channel with two ‘‘stable’’ particles (*e.g.*,  $\gamma N$ ,  $\pi N$ ,  $\eta N$ , or  $K\Lambda$ ), the phase-space factor is parametrized as

$$\delta_i(W) = \frac{q_i}{W} B_{\ell_i}^2(q_i R), \quad (\text{A16})$$

where  $q_i$  is the linear momentum of the two particles in their center-of-momentum frame,  $B_{\ell_i}$  is a Blatt-Weisskopf barrier penetration factor [29], and  $\ell_i$  is the orbital angular momentum of the two particles. The range parameter  $R$  was fixed at 1 fm. If the masses of the two particles in the  $i$ -th channel are  $m$  and  $M$ , then the c.m. energy is

$$W = \sqrt{q_i^2 + m^2} + \sqrt{q_i^2 + M^2}, \quad (\text{A17})$$

which gives

$$q_i = \frac{\sqrt{[W^2 - (m - M)^2][W^2 - (m + M)^2]}}{2W}. \quad (\text{A18})$$

The first few Blatt-Weisskopf factors are given by [29]

$$\begin{aligned} B_0^2(x) &= 1, \\ B_1^2(x) &= \frac{x^2}{1 + x^2}, \\ B_2^2(x) &= \frac{x^4}{9 + 3x^2 + x^4}, \\ B_3^2(x) &= \frac{x^6}{225 + 45x^2 + 6x^4 + x^6}, \\ B_4^2(x) &= \frac{x^8}{11025 + 1575x^2 + 135x^4 + 10x^6 + x^8}. \end{aligned} \quad (\text{A19})$$

As  $q_i \rightarrow 0$ ,  $B_{\ell_i} \sim (q_i R)^\ell$  and  $\delta_i(W) \sim q_i^{2\ell+1}$ . As  $q_i \rightarrow \infty$ ,  $B_{\ell_i}$  approaches unity and  $\delta_i(W)$  becomes constant. These properties ensure that the energy-dependent partial widths have the proper analytic threshold behavior and also remain finite at large energies.

Resonances do not always decay into channels with two stable particles. Sometimes they decay instead into a stable particle and an isobar, or into two isobars. For a quasi-two-body decay of a resonance into an  $i$ -th channel consisting of a stable particle of mass  $m$  and an isobar (*e.g.*,  $\pi\Delta$  or  $\rho N$ ) of mass  $M$ , the phase-space factor  $\delta_i(W)$  is calculated by averaging the ordinary two-body phase-space factor over the mass of the isobar, which is assumed to decay into stable particles with masses  $m_1$  and  $m_2$ ,

$$\delta_i(W) = \int_{m_1+m_2}^{W-m} \sigma(M) \frac{q_i}{W} B_{\ell_i}^2(q_i R) dM. \quad (\text{A20})$$

Note that  $q_i$  is now a function of  $M$ . For simplicity, the distribution function  $\sigma(M)$  is parametrized by a Breit-Wigner lineshape,

$$\sigma(M) = \frac{1}{\pi} \frac{\Gamma/2}{(M - M_0)^2 + (\Gamma/2)^2}, \quad (\text{A21})$$

where here  $M_0$  and  $\Gamma$  are the nominal mass and width of the isobar. In establishing the integration limits, we consider the expression for the mass of the isobar  $M$  as a function of the masses of its decay products,  $m_1$  and  $m_2$ , and their relative c.m. momentum  $q_{12}$ :

$$M = \sqrt{q_{12}^2 + m_1^2} + \sqrt{q_{12}^2 + m_2^2}. \quad (\text{A22})$$

To get the lower limit, observe that the minimum value of  $M$  coincides with the value  $q_{12} = 0$ . This yields the lower integration limit of  $M_{\min} = m_1 + m_2$ . The maximum value of  $M$  must coincide with the maximum value of  $q_{12}$ . Now  $(q_{12})_{\max}$  occurs when  $q_i = 0$  in Eq. (A17), giving the upper integration limit  $M_{\max} = W - m$ . The integration was carried out numerically using Simpson's rule.

For a quasi-two-body decay of a resonance into an  $i$ -th channel consisting of two isobars (*e.g.*,  $\rho\Delta$ ),  $\delta_i(W)$  is calculated by averaging the ordinary two-body phase-space factor over the masses  $M_1$  and  $M_2$  of each of the isobars assumed to decay into stable particles with masses  $m_1$ ,  $m_2$  and  $m_3$ ,  $m_4$ , respectively. This leads to the double integral,

$$\delta_i(W) = \int_{m_1+m_2}^{W-m_3-m_4} \int_{m_3+m_4}^{W-M_1} \sigma(M_1)\sigma(M_2) \frac{q_i}{W} B_{\ell_i}^2(q_i R) dM_2 dM_1. \quad (\text{A23})$$

Here,  $q_i$  is a function of  $M_1$  and  $M_2$ . Again, such integrals were calculated numerically using Simpson's rule.

## 5. Background Parametrization

Background contributions may either arise from attractive or repulsive interactions. In the KSU model, the background matrix  $\mathbf{B}$  is constructed as the product of a small number of symmetric, unitary matrices:  $\mathbf{B} = \mathbf{B}_1 \mathbf{B}_1 \cdots \mathbf{B}_m$ . Each matrix  $\mathbf{B}_i$  may be used to construct a contribution to the background  $S$ -matrix by writing

$$\mathbf{S}_i = (\mathbf{B}_i)^2 = \mathbf{I} + 2i\mathbf{T}_i, \quad (\text{A24})$$

where  $\mathbf{T}_i$  is the  $i$ -th background  $T$ -matrix. Elements of  $\mathbf{T}_i$  are parametrized as

$$(\mathbf{T}_i)_{jk} = \frac{\frac{1}{2}\sqrt{\Gamma_j \Gamma_k}}{\pm M \pm W - i\Gamma/2} = x_j x_k \sin \alpha e^{i\alpha}, \quad (\text{A25})$$

where

$$x_j^2 = \frac{\Gamma_j}{\Gamma}, \quad x_k^2 = \frac{\Gamma_k}{\Gamma}, \quad (\text{A26})$$

and here  $\alpha$  is defined such that

$$\tan \alpha = \pm \frac{\Gamma/2}{M + W}. \quad (\text{A27})$$

The ‘‘partial widths’’  $\Gamma_j$  and  $\Gamma_k$  are parametrized with the same energy dependence as the resonant partial widths discussed in the preceding subsection and  $\Gamma = \sum_j \Gamma_j$  is the corresponding energy-dependent total width. The positive (negative) sign in Eq. (A27) ensures attractive (repulsive) background, where attractive (repulsive) background is characterized by counter-clockwise (clockwise) motion of  $\mathbf{T}_i$  on an Argand diagram. Values of the background ‘‘mass’’ terms,  $M$  in Eq. (A27) were typically kept large ( $M > 10^4$  MeV), which corresponds to a ‘‘distant poles’’ approximation for the background. If we define  $\mathbf{X}\mathbf{X}$  as the matrix having elements  $\mathbf{X}\mathbf{X}_{jk} = x_j x_k$ , then we can write

$$\mathbf{T}_i = \mathbf{X}\mathbf{X} \sin \alpha e^{i\alpha}, \quad (\text{A28})$$

so that the corresponding background  $S$ -matrix is

$$\mathbf{S}_i = \mathbf{I} + 2i\mathbf{X}\mathbf{X} \sin \alpha e^{i\alpha} = \mathbf{I} + \mathbf{X}\mathbf{X}(e^{2i\alpha} - 1) = e^{2i\alpha} \mathbf{X}\mathbf{X}. \quad (\text{A29})$$

The unitarity of  $\mathbf{S}_i$  is ensured by the properties of the basis matrix  $\mathbf{X}\mathbf{X}$ . Note that  $(\mathbf{X}\mathbf{X})^2 = \mathbf{X}\mathbf{X}$ . It follows that the original background matrix contribution  $\mathbf{B}_i$  can be written as

$$\mathbf{B}_i = e^{i\alpha} \mathbf{X}\mathbf{X} = \mathbf{I} + \mathbf{X}\mathbf{X}(e^{i\alpha} - 1). \quad (\text{A30})$$

## Appendix B: Resonance Parameters and Argand Diagrams

Tables VII, VIII, and IX of Appendix B list the partial widths ( $\Gamma_i$ ), branching fractions ( $\mathcal{B}_i$ ), and resonant amplitudes ( $\sqrt{x x_i}$ ) for the isospin-1/2 and isospin-3/2 amplitudes. Figures 1 - 27 show Argand diagrams of the dimensionless energy-dependent amplitudes (solid black curves) fitted to the final single-energy results (data points). Small filled black circles mark the c.m. energies in which resonances were found. The diagrams show the real and imaginary parts of the amplitudes as well as a polar plot of the amplitude from threshold up to 2100 MeV or 2300 MeV. The bottom right corner shows the reaction, the name of the amplitude, and for the photoproduction amplitudes whether it is an electric ( $E$ ) or magnetic ( $M$ ) multiple. Note that for  $I = 1/2$  amplitudes,  $S_{11}(E) = E_{0+}$ ,  $P_{11}(M) = M_{1-}$ ,  $P_{13}(E) = E_{1+}$ ,  $P_{13}(M) = M_{1+}$ ,  $D_{13}(E) = E_{2-}$ ,  $D_{13}(M) = M_{2-}$ ,  $D_{15}(E) = E_{2+}$ ,  $D_{15}(M) = M_{2+}$ ,  $F_{15}(E) = E_{3-}$ ,  $F_{15}(M) = M_{3-}$ ,  $G_{17}(E) = E_{3+}$ ,  $G_{17}(M) = M_{3+}$ , and similarly for  $I = 3/2$  amplitudes. For small amplitudes, the amplitude is shown after scaling. The scaling factor is shown after the amplitude name. Dummy channels for reactions without data or single-energy fits were included to satisfy  $S$ -matrix unitarity. Numerical data for the dimensionless single-energy  $\gamma p \rightarrow \eta p$ ,  $\gamma n \rightarrow \eta n$ , and  $\gamma p \rightarrow K^+ \Lambda$  amplitudes, and for the updated  $\pi^- p \rightarrow \eta n$  and  $\pi^- p \rightarrow K^0 \Lambda$  amplitudes are available in the supplemental data file [30].

Channel	$\Gamma_i$ (MeV)	$\mathcal{B}_i$	$\sqrt{\mathbf{x}\mathbf{x}_i}$	Channel	$\Gamma_i$ (MeV)	$\mathcal{B}_i$	$\sqrt{\mathbf{x}\mathbf{x}_i}$
$S_{11}(1535)$ ****				$S_{11}(1650)$ ****			
$\pi N$	62(3)	42(2)	+0.42(2)	$\pi N$	86(6)	64(4)	+0.64(4)
$\eta N$	63(5)	43(3)	+0.43(1)	$\eta N$	1.0(8)	0.8(6)	+0.07(3)
$K\Lambda$				$K\Lambda$	5(3)	3.5(2)	-0.15(4)
$(\pi\Delta)_D$	< 1.7	< 1.1	-0.043(35)	$(\pi\Delta)_D$	< 0.3	< 0.2	-0.01(8)
$(\rho_3 N)_D$	< 0.5	< 0.3	+0.025(15)	$(\rho_3 N)_D$	20(5)	15(3)	+0.31(3)
$\rho_1 N$	20(3)	14(2)	-0.24(2)	$\rho_1 N$	< 5	1.8(1.7)	+0.11(5)
$\epsilon N$	< 1.5	< 1	-0.04(4)	$\epsilon N$	16(5)	12(4)	+0.28(4)
$\pi N^*$	< 0.01	< 0.01	+0.003(2)	$\pi N^*$	3(2)	2(1)	+0.12(3)
$S_{11}(1895)$ ****				$P_{11}(1440)$ ****			
$\pi N$	39(18)	8(4)	+0.08(4)	$\pi N$	153(10)	59(2)	+0.59(2)
$\eta N$	174(52)	37(9)	-0.18(5)	$\eta N$			
$K\Lambda$	31(21)	7(4)	+0.07(2)	$K\Lambda$			
$(\pi\Delta)_D$	< 49	< 10	+0.05(5)	$(\pi\Delta)_P$	56(9)	22(4)	+0.36(3)
$(\rho_3 N)_D$	105(45)	23(9)	+0.14(4)	$\rho_1 N$	< 0.003	0.00(0)	-0.00(2)
$\rho_1 N$	< 85	< 18	+0.08(5)	$\epsilon N$	41(9)	16(3)	+0.31(3)
$\epsilon N$	< 59	< 13	-0.08(4)				
$\pi N^*$	34(24)	7(5)	-0.08(4)				
$P_{11}(1710)$ ****				$P_{11}(1880)$ ***			
$\pi N$	23(13)	12(6)	+0.12(6)	$\pi N$	125(42)	25(6)	+0.25(6)
$\eta N$	33(19)	17(8)	-0.14(4)	$\eta N$	11(6)	2(1)	-0.07(2)
$K\Lambda$	3.5(3)	1.8(1.5)	+0.05(2)	$K\Lambda$	11(5)	2(1)	-0.075(20)
$(\pi\Delta)_D$	55(21)	28(9)	+0.19(4)	$(\pi\Delta)_D$	57(31)	11(6)	-0.17(5)
$\rho_1 N$	34(17)	17(9)	-0.14(5)	$\rho_1 N$	160(62)	32(13)	+0.29(4)
$\epsilon N$	< 33	< 16	-0.10(5)	$\epsilon N$	< 45	< 9	-0.09(7)
$P_{11}(2100)$ ***				$P_{13}(1720)$ ****			
$\pi N$	117(58)	21(11)	+0.21(11)	$\pi N$	41(4)	18(2)	+0.178(16)
$\eta N$	< 25	< 4.7	-0.06(5)	$\eta N$	8.7(1.6)	3.8(5)	+0.082(7)
$K\Lambda$	< 5.4	< 1.0	+0.024(3)	$K\Lambda$	37(7)	16(3)	-0.17(1)
$(\pi\Delta)_D$	< 40	< 7.5	-0.06(11)				
$\rho_1 N$	284(140)	52(19)	-0.33(8)				
$\epsilon N$	< 190	< 35	-0.17(12)				
$P_{13}(1900)$ ****				$P_{13}(2040)$ *			
$\pi N$	5.7(2.9)	1.9(1)	+0.019(10)	$\pi N$	89(25)	16.7(1)	+0.17(4)
$\eta N$	3.8(1.4)	1.3(5)	-0.016(3)	$\eta N$	73(27)	14	-0.15(4)
$K\Lambda$	40(8)	13.7(3)	-0.052(16)	$K\Lambda$	< 0.7	< .04	+0.004(29)
$\rho_1 N$	94(20)	32(7)	+0.079(19)	$\rho_1 N$	52(40)	10(1)	+0.127(4)

TABLE VII. Below each resonance name are listed coupling partial widths ( $\Gamma_i$ ), branching fractions ( $\mathcal{B}_i$ ), and resonant amplitudes ( $\sqrt{\mathbf{x}\mathbf{x}_i}$ ) for the channels listed in columns one and five. For a given resonance, the partial widths and quantities directly derived from them (e.g., branching fractions and resonant amplitudes) were all calculated from energy-dependent partial widths evaluated at the Breit-Wigner mass of the resonance. Star rating is that found in the *Review of Particle Physics* (RPP) [23]. Table contains couplings to  $S_{11}$ ,  $P_{11}$ ,  $P_{13}$  resonances included in the fits.

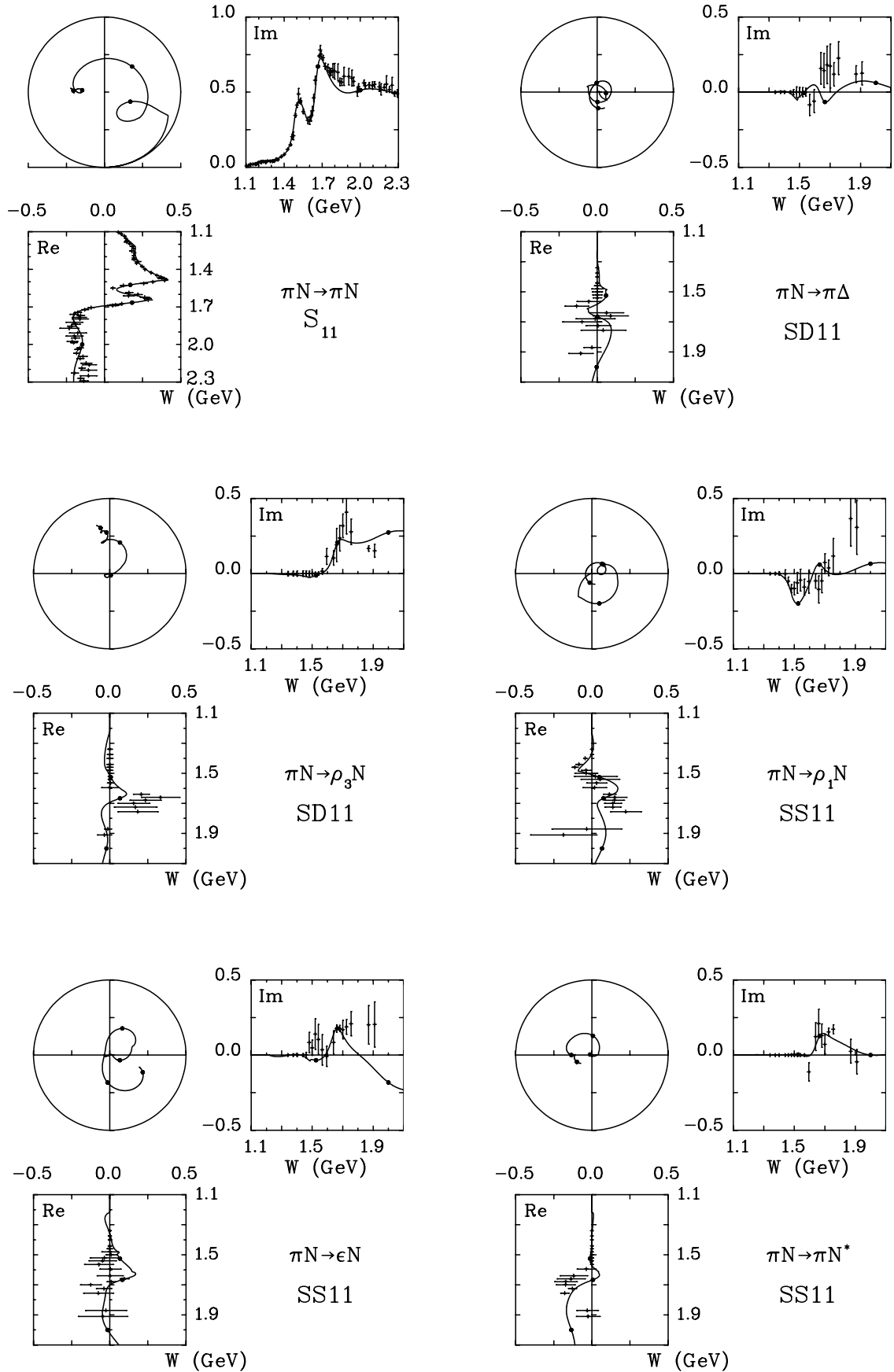


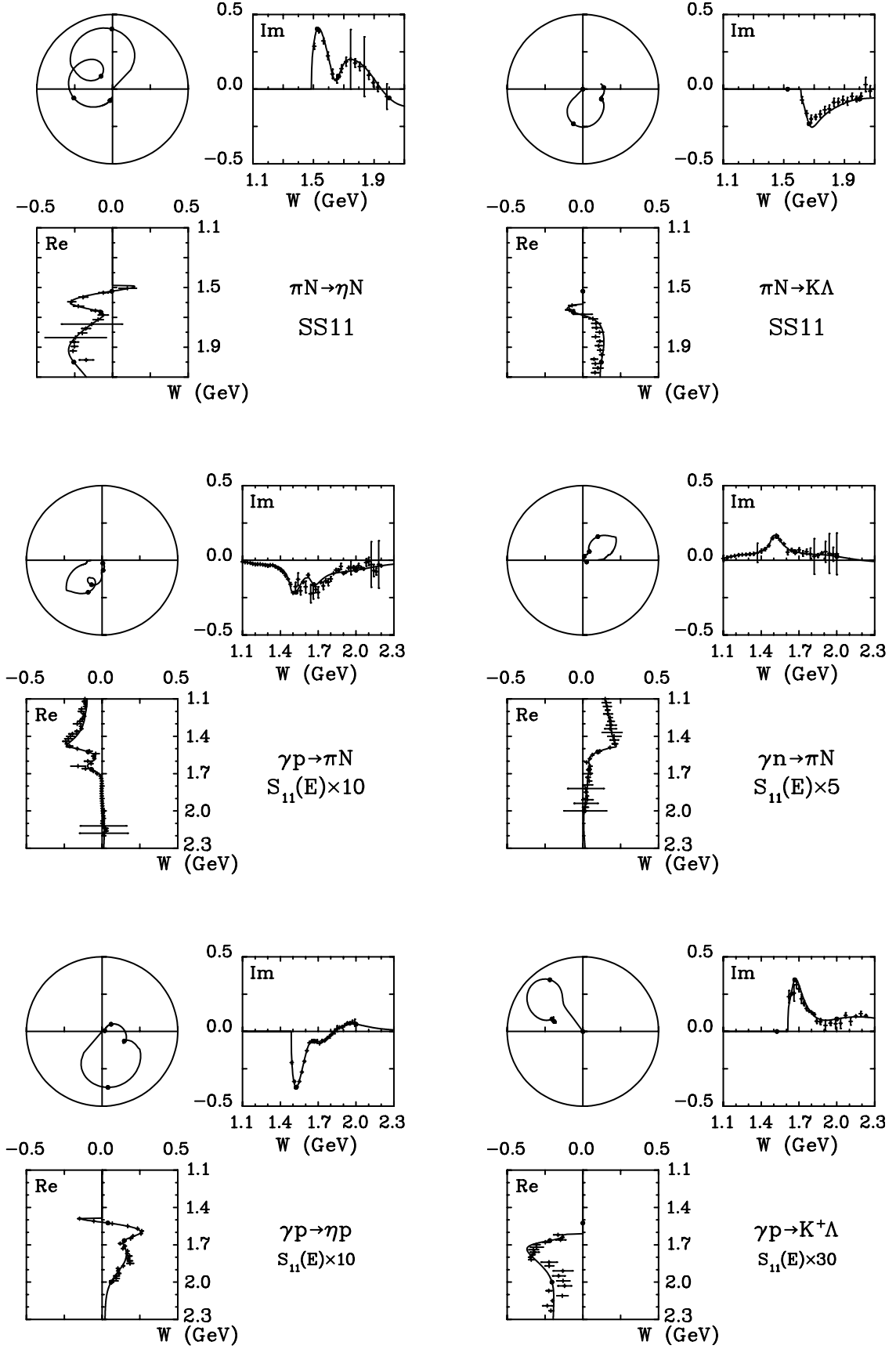
Channel	$\Gamma_i$ (MeV)	$\mathcal{B}_i$	$\sqrt{\mathbf{x}\mathbf{x}_i}$	Channel	$\Gamma_i$ (MeV)	$\mathcal{B}_i$	$\sqrt{\mathbf{x}\mathbf{x}_i}$
$D_{13}(1520)$ ****				$D_{13}(1700)$ ***			
$\pi N$	71(2)	58.3(1.5)	+0.58(2)	$\pi N$	3.0(1)	3.7(1)	+0.037(10)
$\eta N$	0.041(8)	0.03(1)	+0.014(2)	$\eta N$	0.9(5)	1.1(6)	+0.020(6)
$K\Lambda$				$K\Lambda$	1.1(5)	1.3(7)	-0.022(6)
$(\pi\Delta)_S$	25(3)	21(2)	-0.35(2)	$(\pi\Delta)_S$	9(6)	11(8)	+0.06(2)
$(\pi\Delta)_D$	7.2(1.2)	6(1)	-0.19(1)	$(\pi\Delta)_D$	10.4(6.5)	13(5)	+0.07(2)
$(\rho_3 N)_S$	17.1(1.9)	14.1(1.5)	-0.29(2)	$(\rho_3 N)_S$	6(3)	7.5(3.6)	-0.05(2)
$\epsilon N$	< 0.9	< 0.7	-0.04(3)	$\epsilon N$	50(10)	62(9)	+0.15(2)
$D_{13}(1875)$ ***				$D_{13}(2120)$ ***			
$\pi N$	24(5)	7.5(1)	+0.075(14)	$\pi N$	97(14)	19(2)	+0.19(2)
$\eta N$	10.6(2.6)	3.3(8)	+0.050(8)	$\eta N$	16(12)	3.1(2.4)	-0.08(3)
$K\Lambda$	3.6(1.4)	1.1(4)	+0.029(5)	$K\Lambda$	43(14)	8.5(2.5)	-0.13(2)
$(\pi\Delta)_S$	< 6	< 2	+0.017(34)	$(\pi\Delta)_S$	125(59)	25(11)	-0.22(4)
$(\pi\Delta)_D$	54(21)	17(6)	-0.11(2)	$(\pi\Delta)_D$	171(62)	34(11)	+0.26(5)
$(\rho_3 N)_S$	147(36)	46(10)	+0.19(2)	$(\rho_3 N)_S$	< 16	< 3	+0.044(48)
$\epsilon N$	78(27)	24.3(8.6)	-0.135(30)	$\epsilon N$	46(26)	9(5)	-0.13(4)
$D_{15}(1675)$ ****				$D_{15}(2060)$ ***			
$\pi N$	53(3)	33(1)	+0.33(1)	$\pi N$	26(6)	5.3(1.4)	+0.05(1)
$\eta N$	3.3(5)	2.0(3)	-0.082(7)	$\pi N$	26(6)	5.3(1.4)	+0.05(1)
$K\Lambda$	< 0.06	< 0.04	-0.007(5)	$K\Lambda$	76(29)	15(5)	+0.09(1)
$(\pi\Delta)_D$	94(6)	58.3(2)	+0.437(5)	$(\pi\Delta)_D$	74(30)	15(6)	+0.09(2)
$\rho_1 N$	< 0.3	< 0.2	-0.017(11)	$\rho_1 N$	21(31)	< 10	+0.047(36)
$(\rho_3 N)_D$	0.6(4)	0.4(3)	-0.036(13)	$(\rho_3 N)_D$	70(43)	14(9)	-0.09(3)
$F_{15}(1680)$ ****				$F_{15}(1860)$ **			
$\pi N$	84(2)	68.0(1)	+0.680(9)	$\pi N$	30(5)	8.0(1)	+0.08(1)
$\eta N$	0.11(3)	0.09(2)	+0.025(3)	$\eta N$	0.4(3)	0.11(9)	+0.009(4)
$K\Lambda$	0.00(0)	0.00(0)	-0.0008(12)	$K\Lambda$	< 0.03	0.00(1)	-0.0015(15)
$(\pi\Delta)_P$	16(2)	13(1)	-0.300(15)	$(\pi\Delta)_P$	39(24)	10(6)	+0.09(3)
$(\pi\Delta)_F$	< 0.4	< 0.3	-0.03(2)	$(\pi\Delta)_F$	102(50)	27(11)	+0.15(3)
$(\rho_3 N)_P$	9.1(1.5)	7(1)	-0.22(2)	$(\rho_3 N)_P$	< 32	< 8.5	+0.05(4)
$(\rho_3 N)_F$	3.0(5)	2.4(4)	-0.128(10)	$(\rho_3 N)_F$	< 0.4	< 0.1	+0.00(3)
$\epsilon N$	11(2)	8.7(1.5)	+0.24(2)	$\epsilon N$	192(41)	51(10)	+0.20(2)
$F_{17}(1990)$ **				$F_{17}(2200)$ new			
$\pi N$	9.4(3)	1.9(4)	+0.019(4)	$\pi N$	45(6)	8.6(8)	+0.086(7)
$\eta N$	8.3(4.5)	1.7(9)	-0.018(5)	$\eta N$	22(11)	4.2(2.3)	+0.06(2)
$K\Lambda$	29(8)	6.0(1)	-0.034(5)	$K\Lambda$	36(9)	7.0(1)	-0.078(6)
$G_{17}(2190)$ ****				$G_{19}(2250)$ ****			
$\pi N$	101(10)	22.9(6)	+0.229(6)	$\pi N$	29(4)	8.5(4)	+0.085(4)
$\eta N$	12(9)	2.7(2.2)	+0.08(3)	$\eta N$	< 17	0.07(5.0)	-0.01(27)
$K\Lambda$	2.5(5)	0.6(1)	-0.036(4)	$K\Lambda$	7(2)	2.0(6)	+0.042(6)
$(\rho_3 N)_D$	< 49	< 11	-0.11(6)				

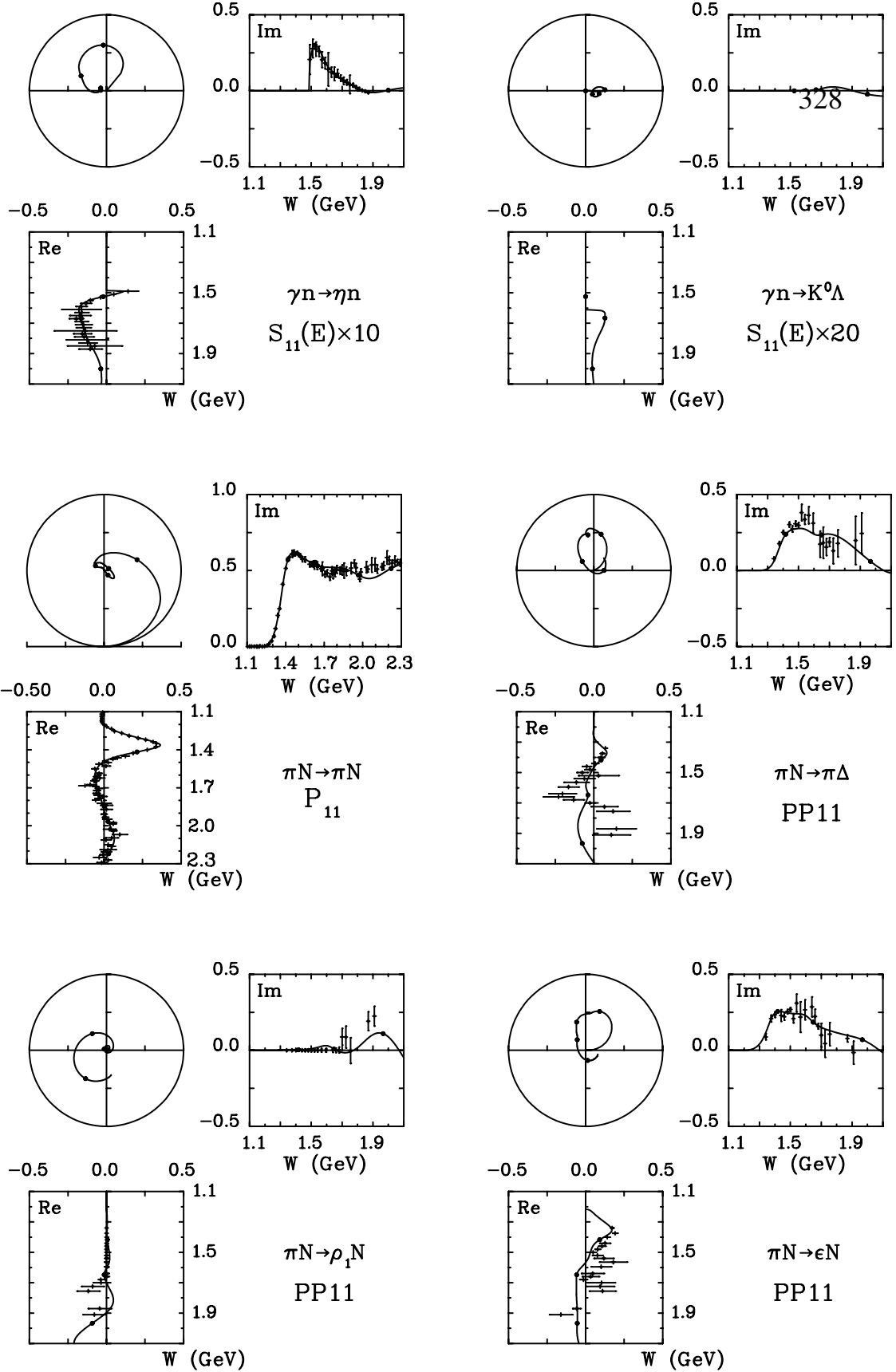
TABLE VIII. Below each resonance name are listed partial widths ( $\Gamma_i$ ), branching fractions ( $\mathcal{B}_i$ ), and resonant amplitudes ( $\sqrt{\mathbf{x}\mathbf{x}_i}$ ) for the channels listed in columns one and five. For a given resonance, the partial widths and quantities directly derived from them (e.g., branching fractions and resonant amplitudes) were all calculated from energy-dependent partial widths evaluated at the Breit-Wigner mass of the resonance. Star rating is that found in the *Review of Particle Physics* (RPP) [22]. Table contains couplings to  $D_{13}$ ,  $D_{15}$ ,  $F_{15}$ ,  $F_{17}$ ,  $G_{17}$ , and  $G_{19}$  resonances included in the fits.

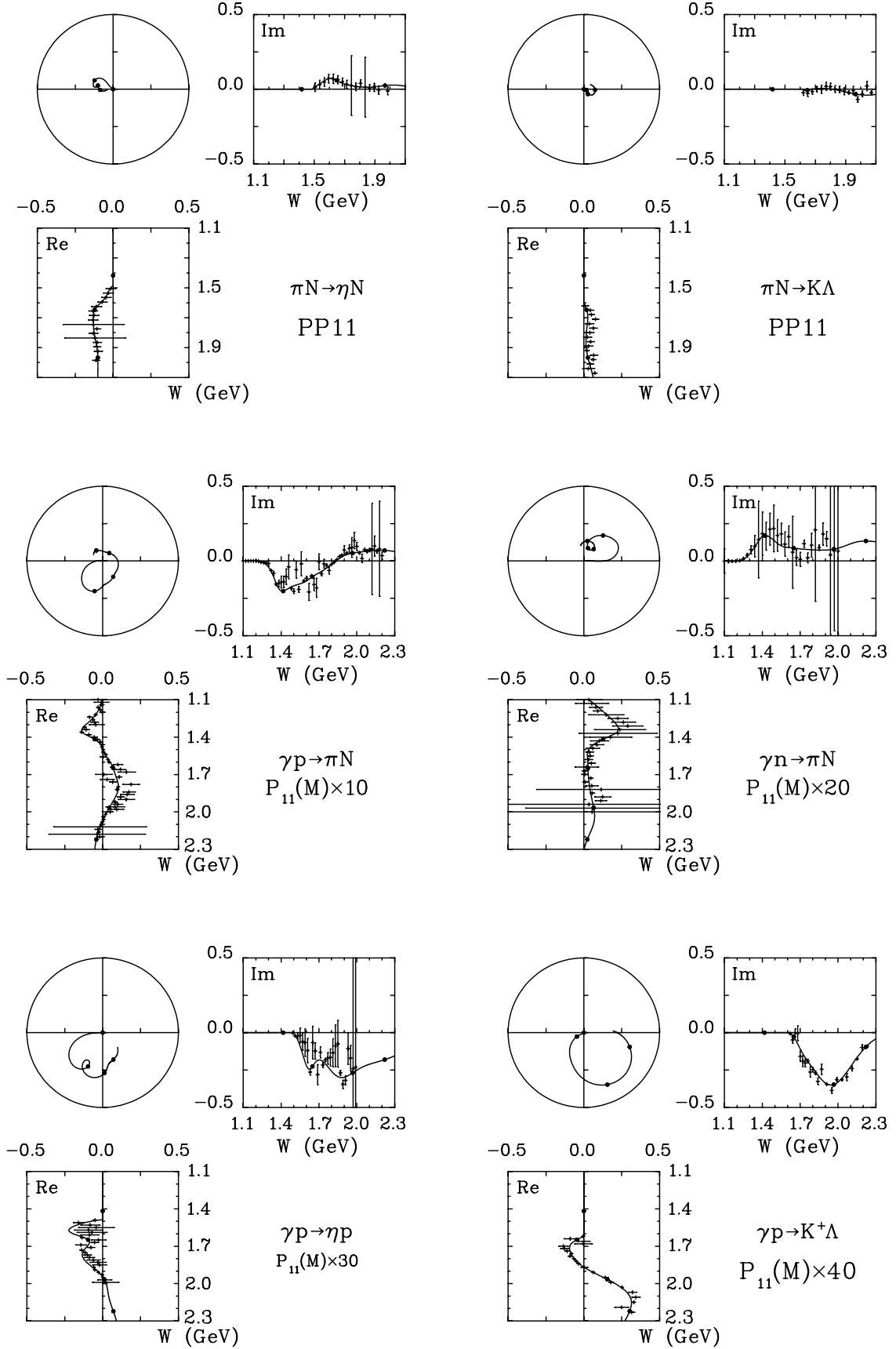
Channel	$\Gamma_i$ (MeV)	$\mathcal{B}_i$	$\sqrt{\mathbf{x}\mathbf{x}_i}$	Channel	$\Gamma_i$ (MeV)	$\mathcal{B}_i$	$\sqrt{\mathbf{x}\mathbf{x}_i}$
$S_{31}(1620)$ ****				$S_{31}(1900)$ ***			
$\pi N$	26(2)	24(2)	+0.24(2)	$\pi N$	17(4)	3.7(8)	+0.037(8)
$(\pi\Delta)_D$	52(6)	48(4)	-0.344(16)	$(\pi\Delta)_D$	192(41)	42(8)	+0.12(2)
$(\rho_3 N)_D$	< 0.05	< 0.04	-0.003(16)	$(\rho_3 N)_D$	83(38)	18(7)	-0.08(2)
$\rho_1 N$	29(4)	27(4)	+0.26(2)	$\rho_1 N$	104(54)	23(12)	+0.09(2)
$\pi N^*$	< 0.02	< 0.02	+0.016(8)	$\pi N^*$	56(41)	12(9)	+0.067(25)
$P_{31}(1910)$ ****				$P_{31}(2250)$ <b>new</b>			
$\pi N$	34(14)	13(3)	+0.13(3)	$\pi N$	45(15)	14(4)	+0.14(4)
$\pi N^*$	87(36)	33(12)	-0.21(5)	$\pi N^*$	150(58)	47(13)	-0.26(6)
$P_{33}(1232)$ ****				$P_{33}(1600)$ ****			
$\pi N$	110.2(8)	99.39(1)	+0.994(1)	$\pi N$	34(8)	10.7(1.9)	+0.107(19)
$(\pi\Delta)_P$	0.0(0)	0.0(0)	+0.00(1)	$(\pi\Delta)_P$	206(28)	64(6)	+0.26(2)
$\pi N^*$	0.0(0)	0.0(0)	+0.00(1)	$\pi N^*$	70(18)	22(5)	+0.15(2)
$P_{33}(1920)$ ***				$D_{33}(1700)$ ****			
$\pi N$	53(25)	10.5(3.0)	+0.10(3)	$\pi N$	34(4)	15(2)	+0.15(2)
$(\pi\Delta)_P$	< 8	< 1.6	-0.017(39)	$(\pi\Delta)_S$	112(13)	49(5)	+0.27(2)
$\pi N^*$	392(94)	77(9)	+0.28(4)	$(\pi\Delta)_D$	17(7)	7.6(3)	-0.11(2)
				$(\rho_3 N)_S$	62(14)	27(5)	+0.20(2)
$D_{33}(1940)$ **				$D_{35}(1930)$ ***			
$\pi N$	62(14)	16(4)	+0.16(4)	$\pi N$	47(13)	9.5(1)	+0.095(10)
$(\pi\Delta)_S$	< 3.6	< 0.9	+0.018(32)				
$(\pi\Delta)_D$	< 25	< 6.3	-0.068(38)				
$(\rho_3 N)_S$	321(47)	80(5)	+0.35(4)				
$F_{35}(1905)$ ****				$F_{37}(1950)$ ****			
$\pi N$	50(5)	17(1)	+0.17(1)	$\pi N$	92(6)	38(2)	+0.383(15)
$(\pi\Delta)_P$	24(15)	8.4(5)	+0.12(4)				
$(\pi\Delta)_F$	140(27)	49(9)	+0.29(3)				
$(\rho_3 N)_P$	74(27)	26(9)	+0.21(4)				

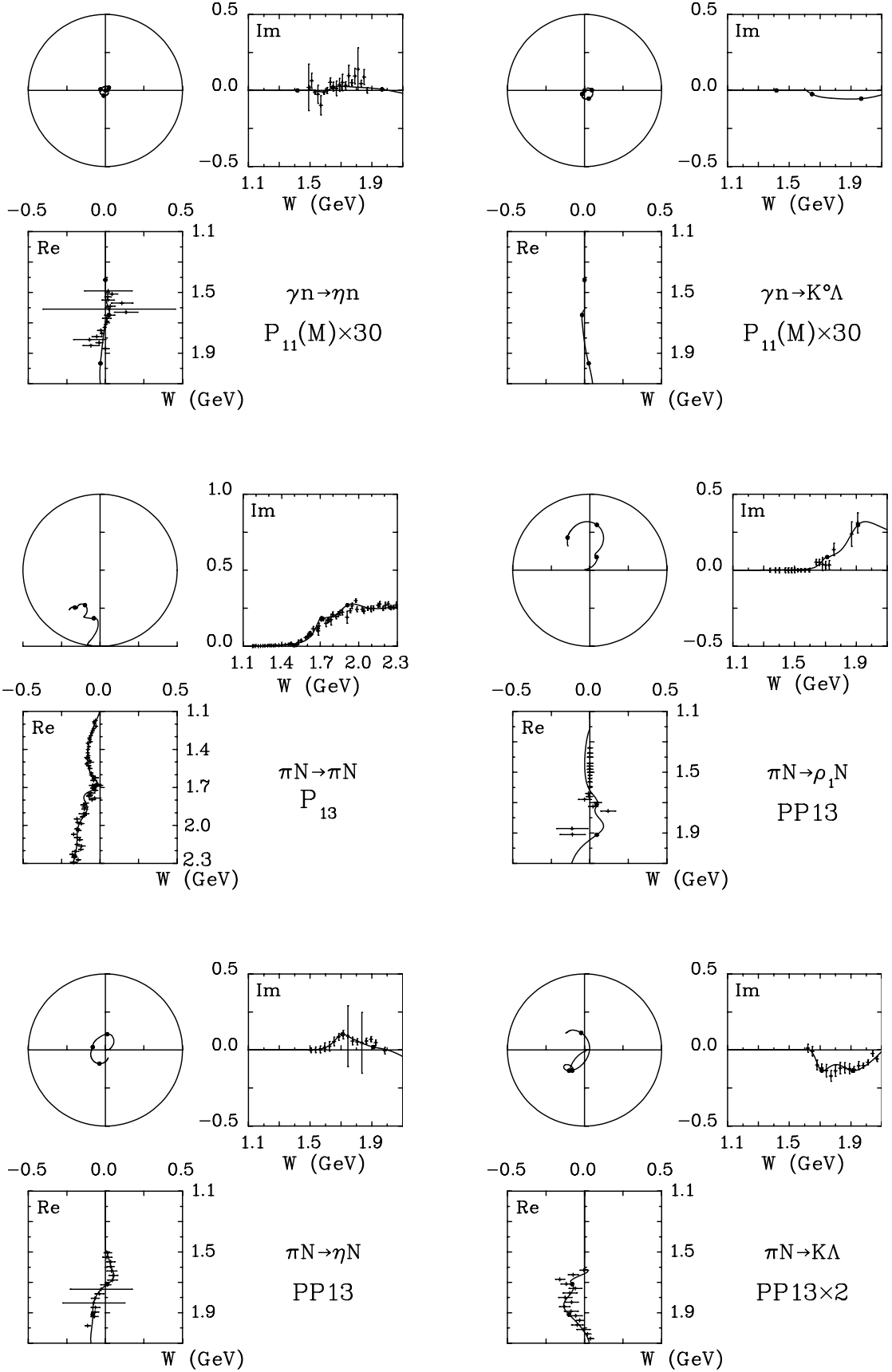
TABLE IX. Below each resonance name are listed partial widths ( $\Gamma_i$ ), branching fractions ( $\mathcal{B}_i$ ), and resonant amplitudes ( $\sqrt{\mathbf{x}\mathbf{x}_i}$ ) for the channels listed in columns one and five. For a given resonance, the partial widths and quantities directly derived from them (e.g., branching fractions and resonant amplitudes) were all calculated from energy-dependent partial widths evaluated at the Breit-Wigner mass of the resonance. Star rating is that found in the *Review of Particle Physics* (RPP) [22]. Table contains couplings to  $S_{31}$ ,  $P_{31}$ ,  $P_{33}$ ,  $D_{33}$ ,  $D_{35}$ ,  $F_{35}$ ,  $F_{37}$  resonances included in the fits.

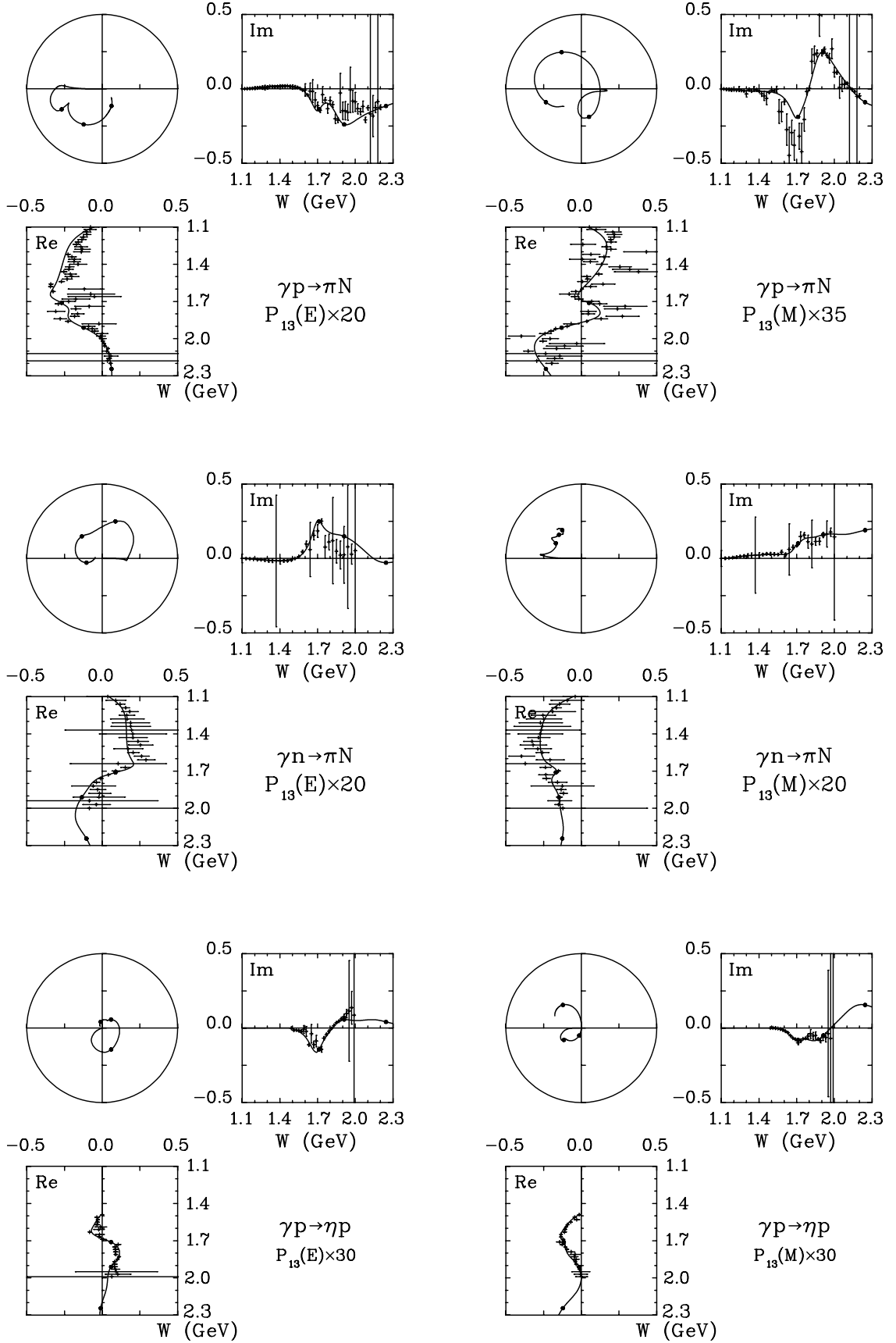
FIG. 1. Argand diagrams for the  $I = 1/2$  amplitudes.

FIG. 2. Argand diagrams for the  $I = 1/2$  amplitudes.

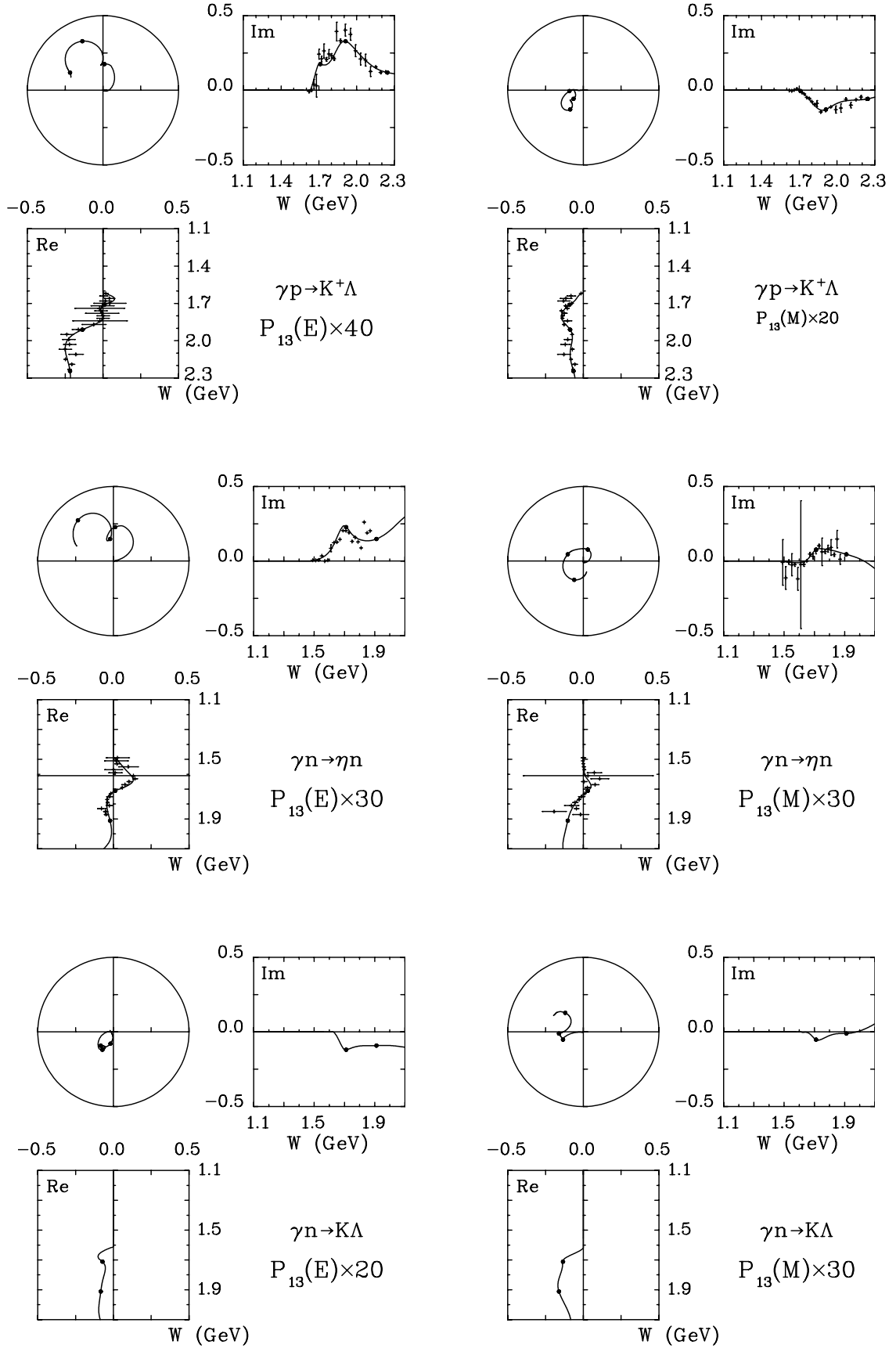
FIG. 3. Argand diagrams for the  $I = 1/2$  amplitudes.

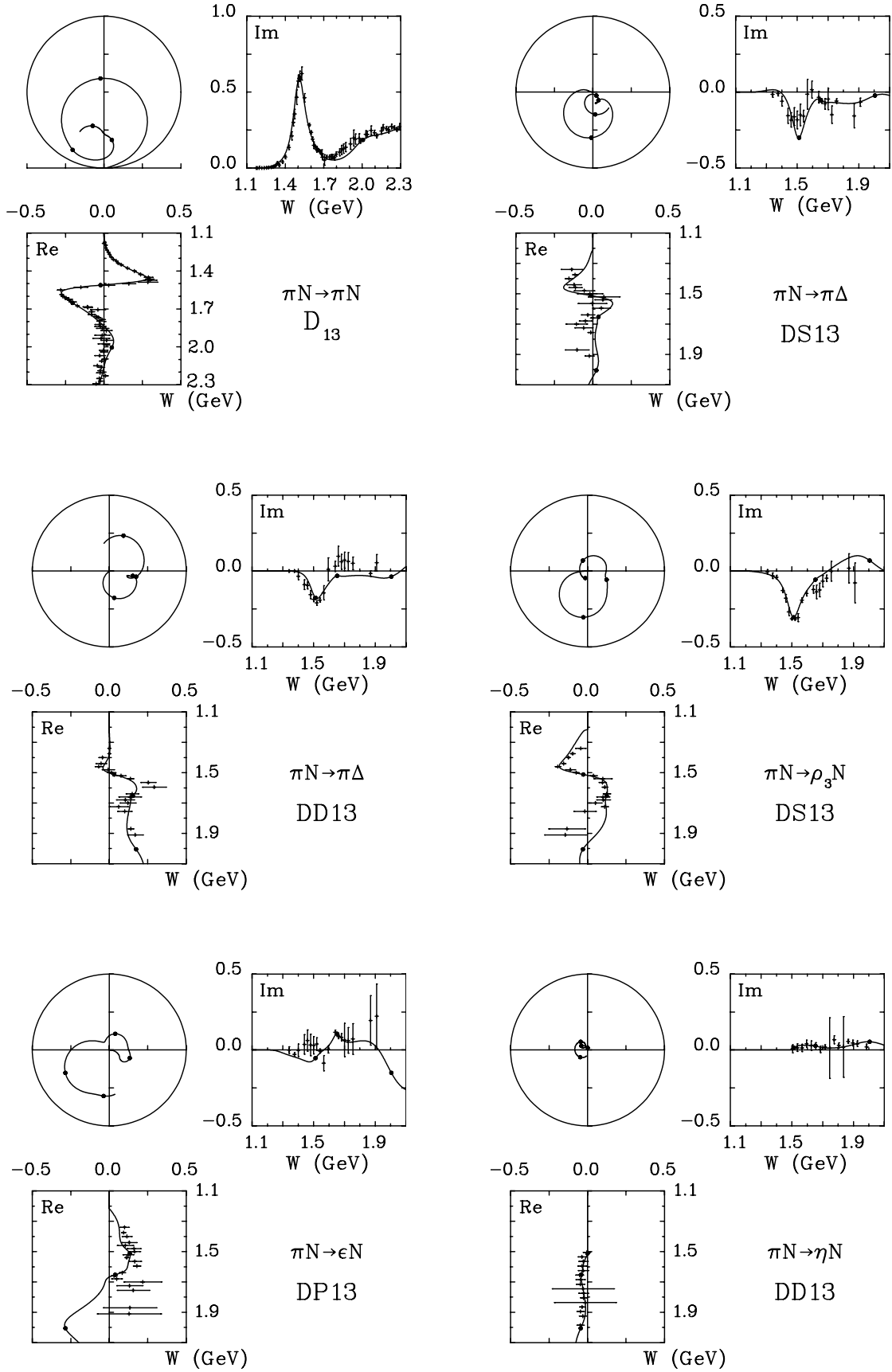
FIG. 4. Argand diagrams for the  $I = 1/2$  amplitudes.

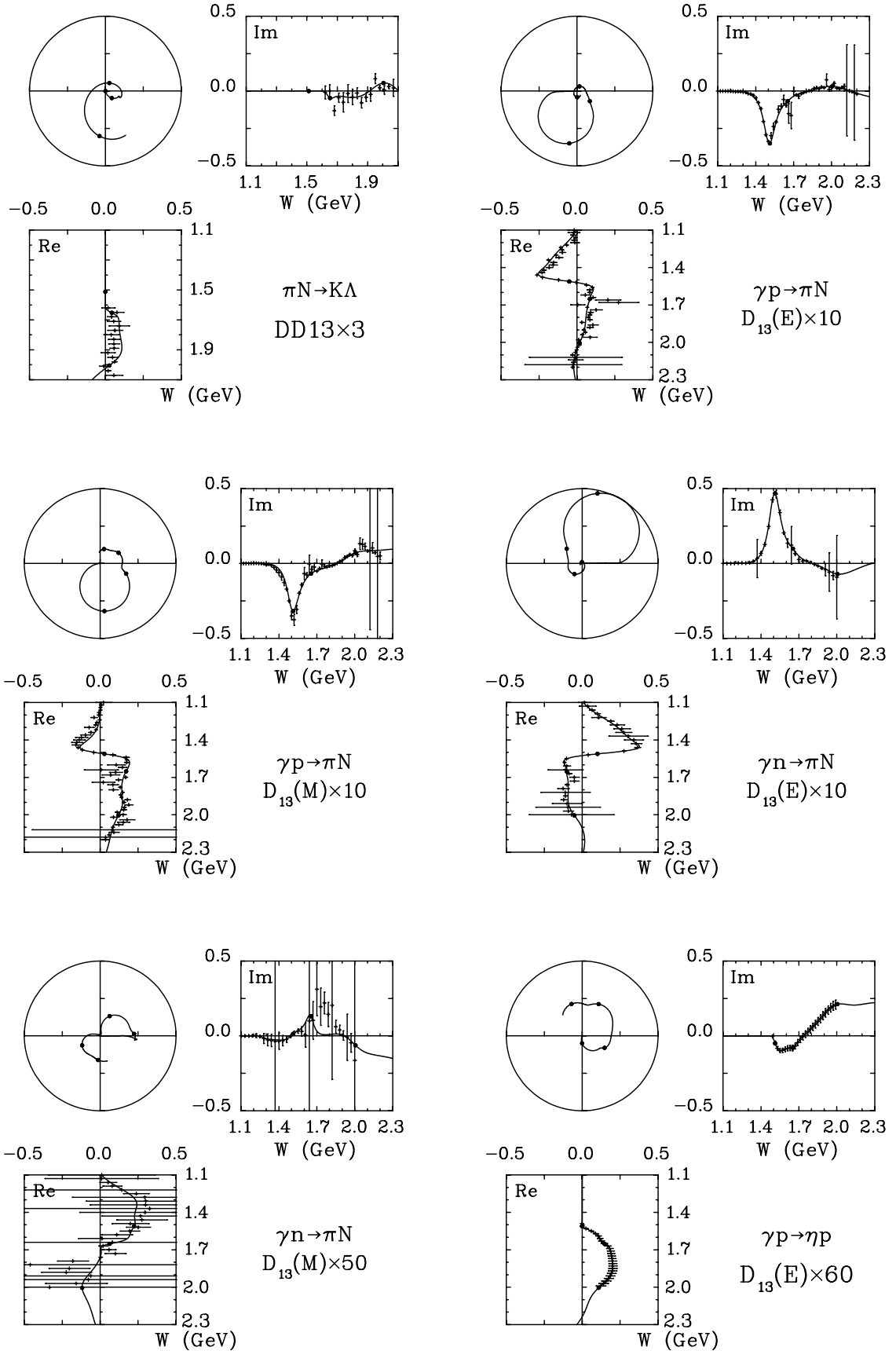
FIG. 5. Argand diagrams for the  $I = 1/2$  amplitudes.

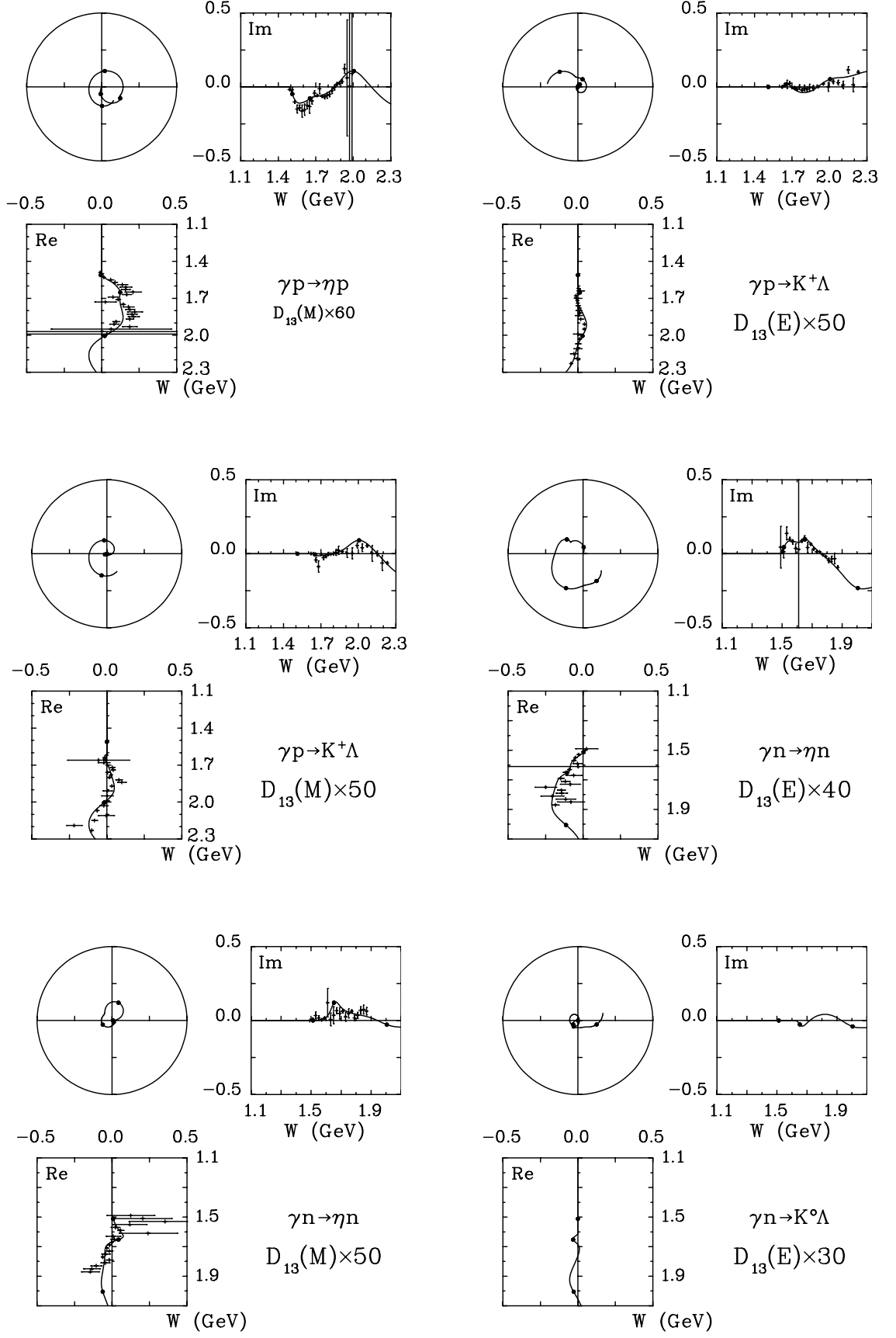
FIG. 6. Argand diagrams for the  $I = 1/2$  amplitudes.

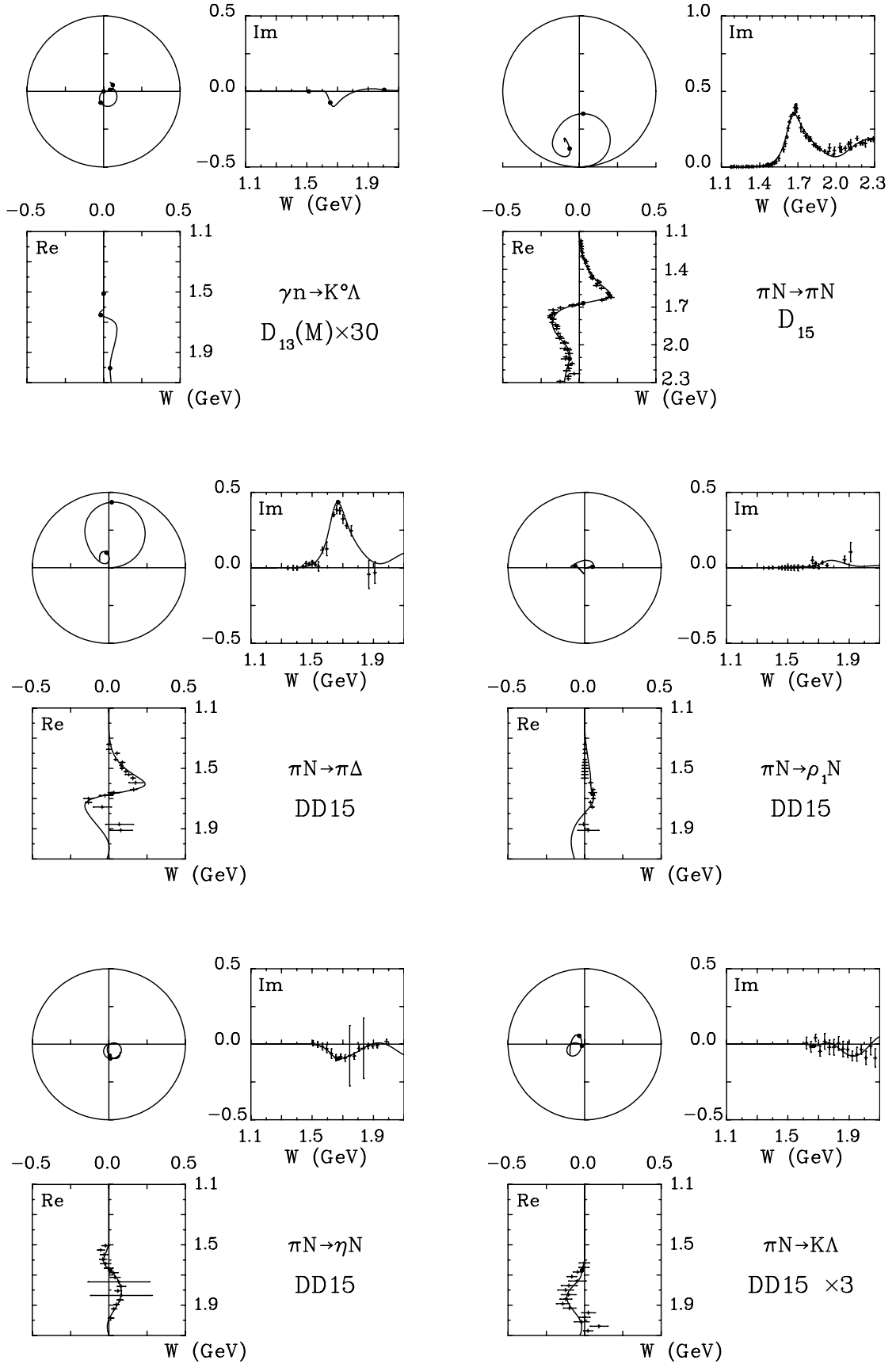


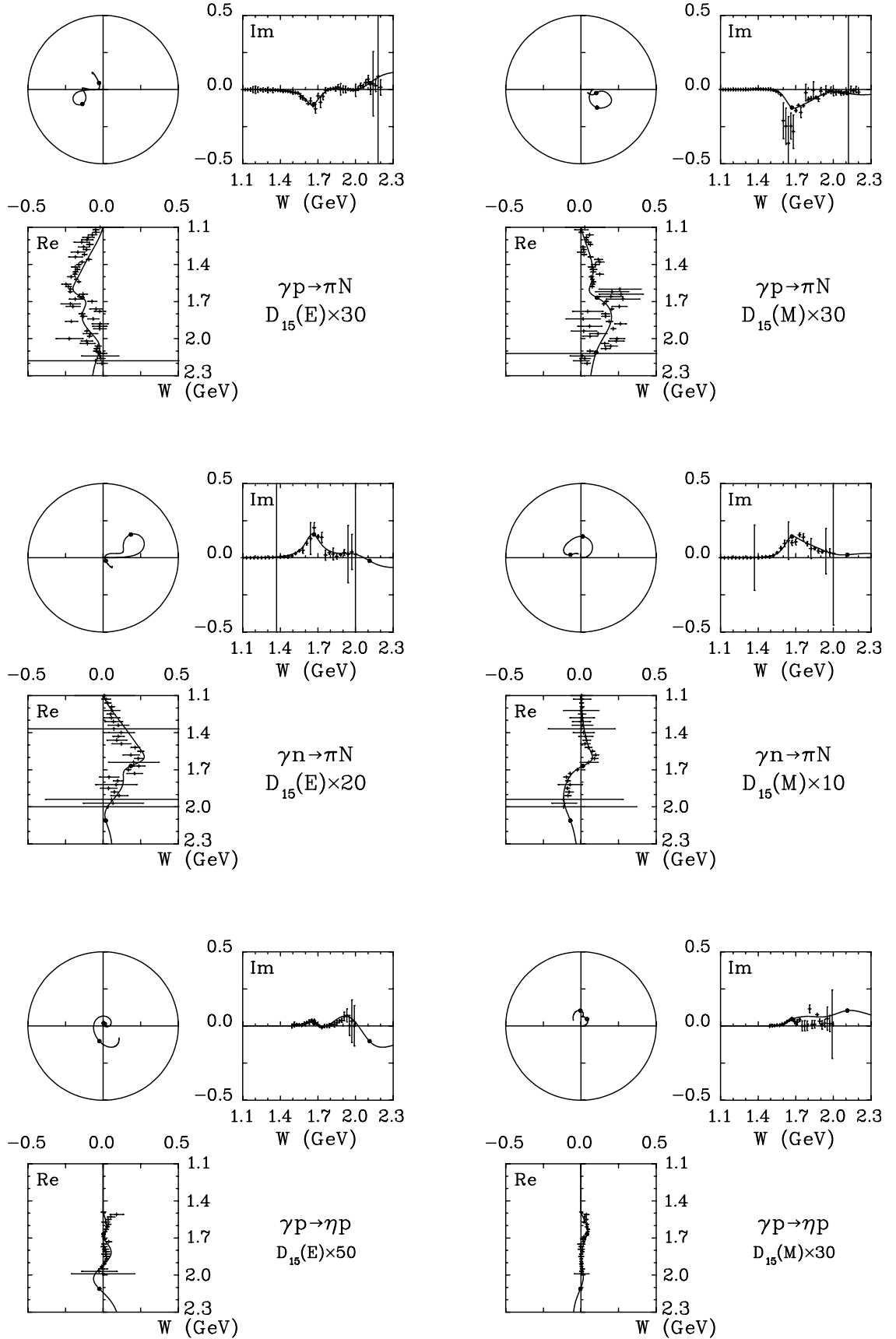
FIG. 7. Argand diagrams for the  $I = 1/2$  amplitudes.

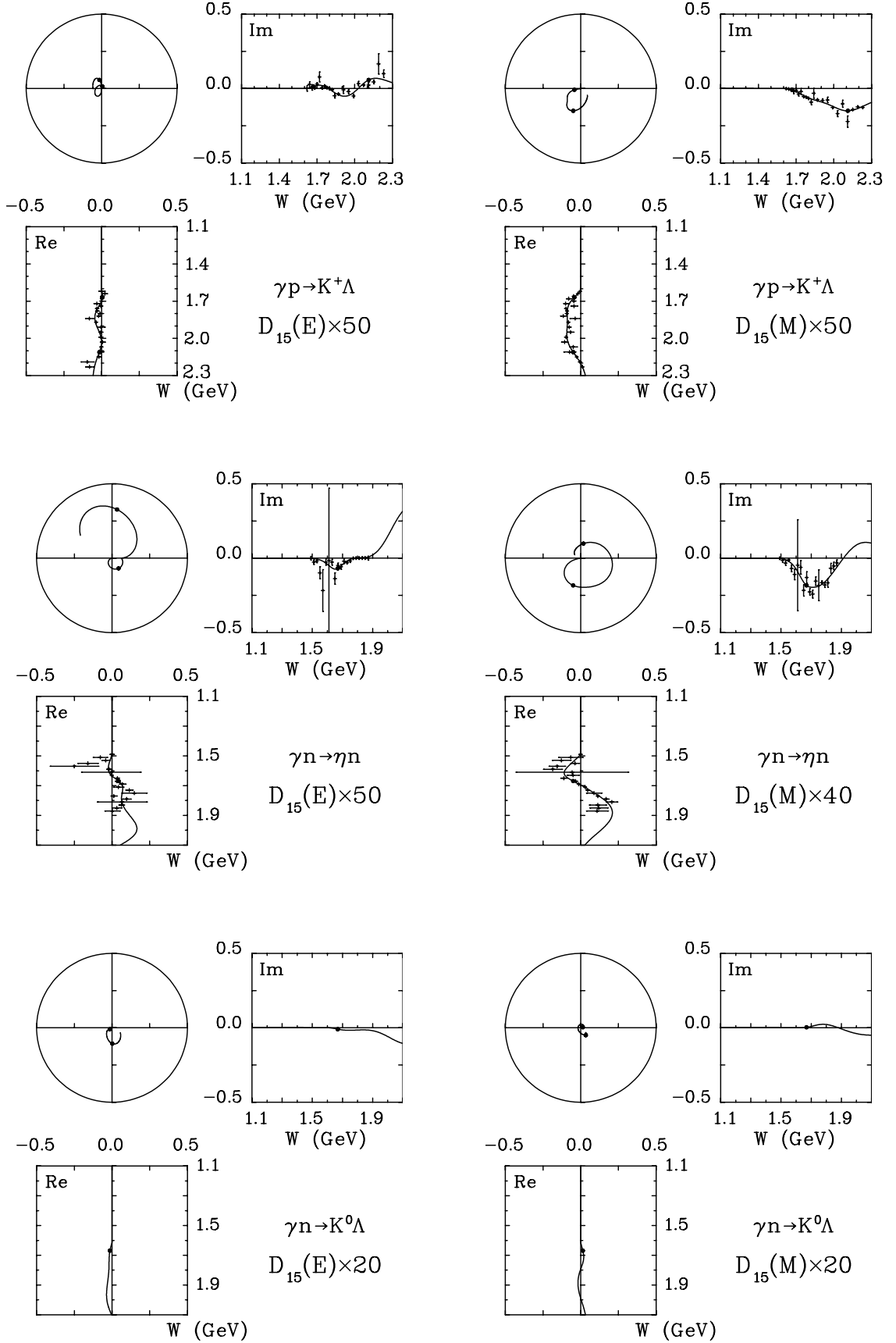
FIG. 8. Argand diagrams for the  $I = 1/2$  amplitudes.

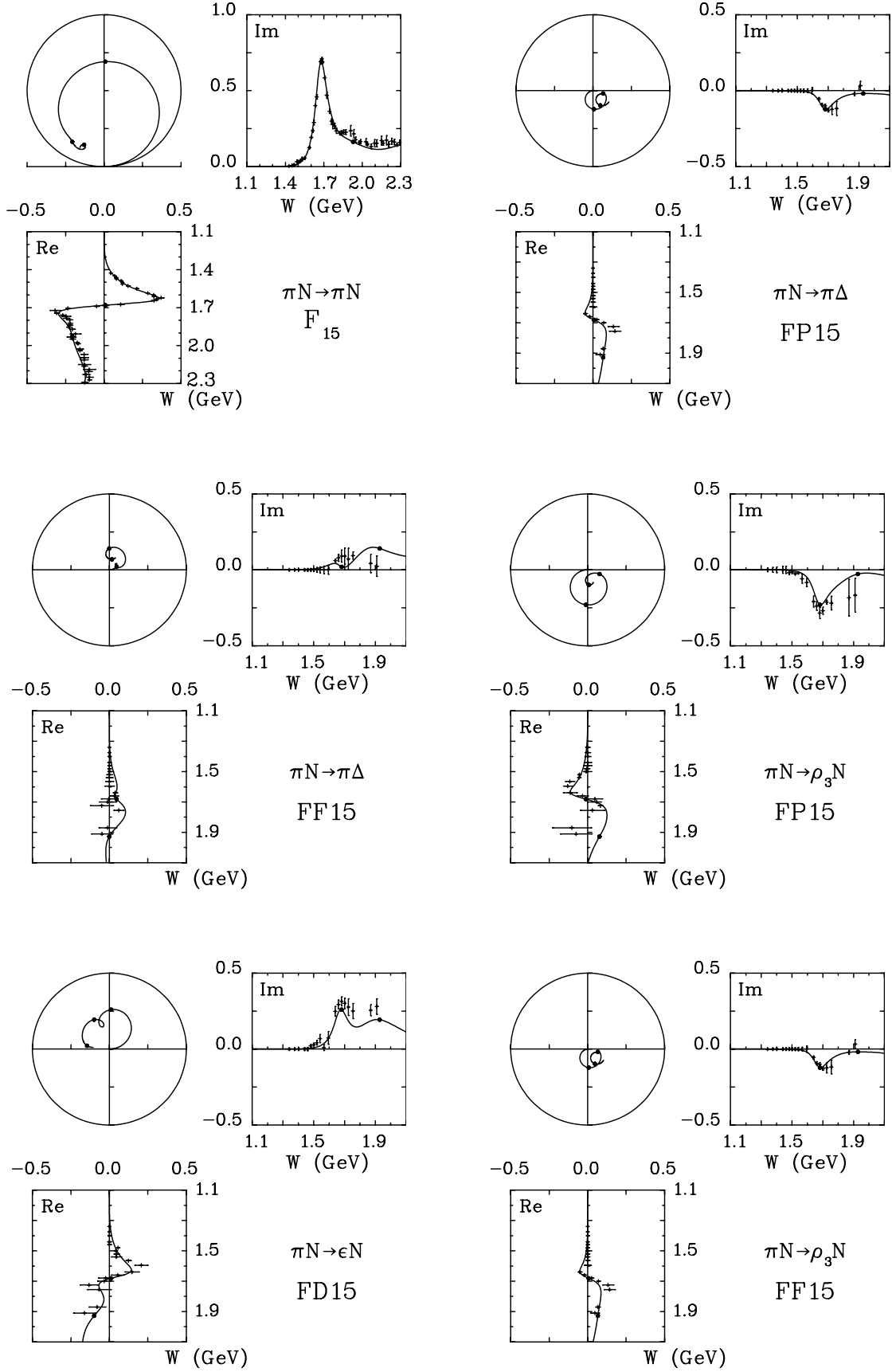
FIG. 9. Argand diagrams for the  $I = 1/2$  amplitudes.

FIG. 10. Argand diagrams for the  $I = 1/2$  amplitudes.

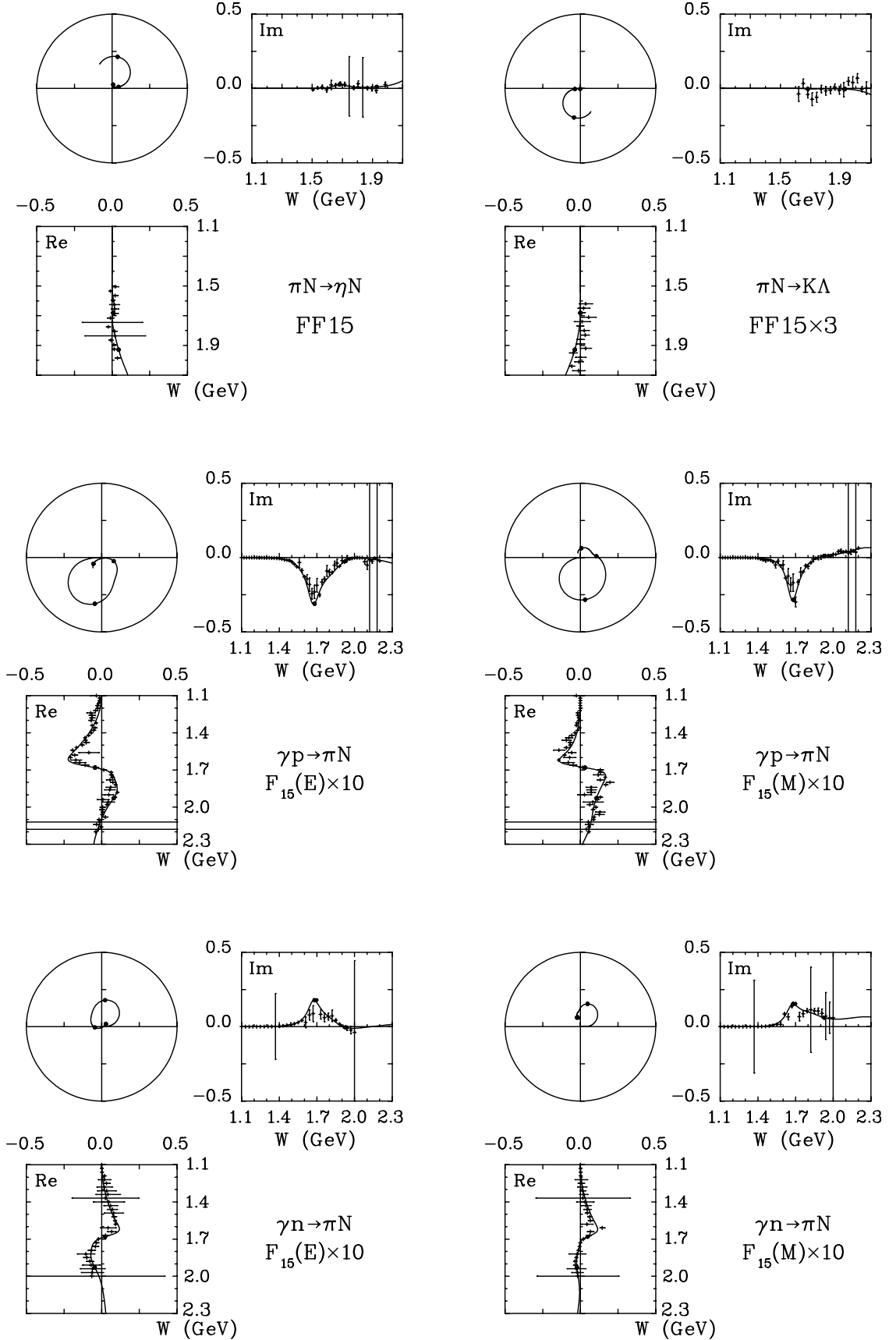
FIG. 11. Argand diagrams for the  $I = 1/2$  amplitudes.

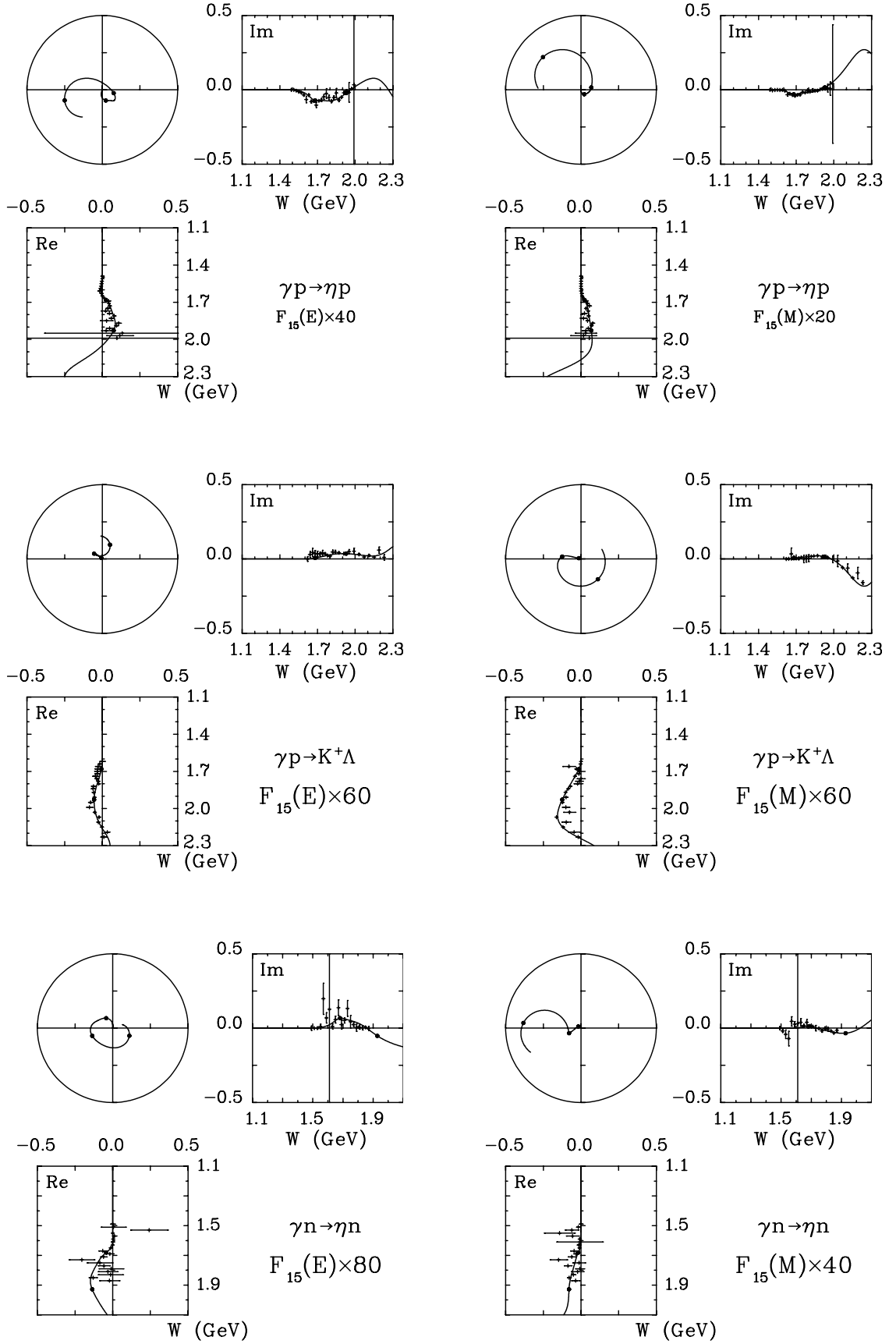
FIG. 12. Argand diagrams for the  $I = 1/2$  amplitudes.

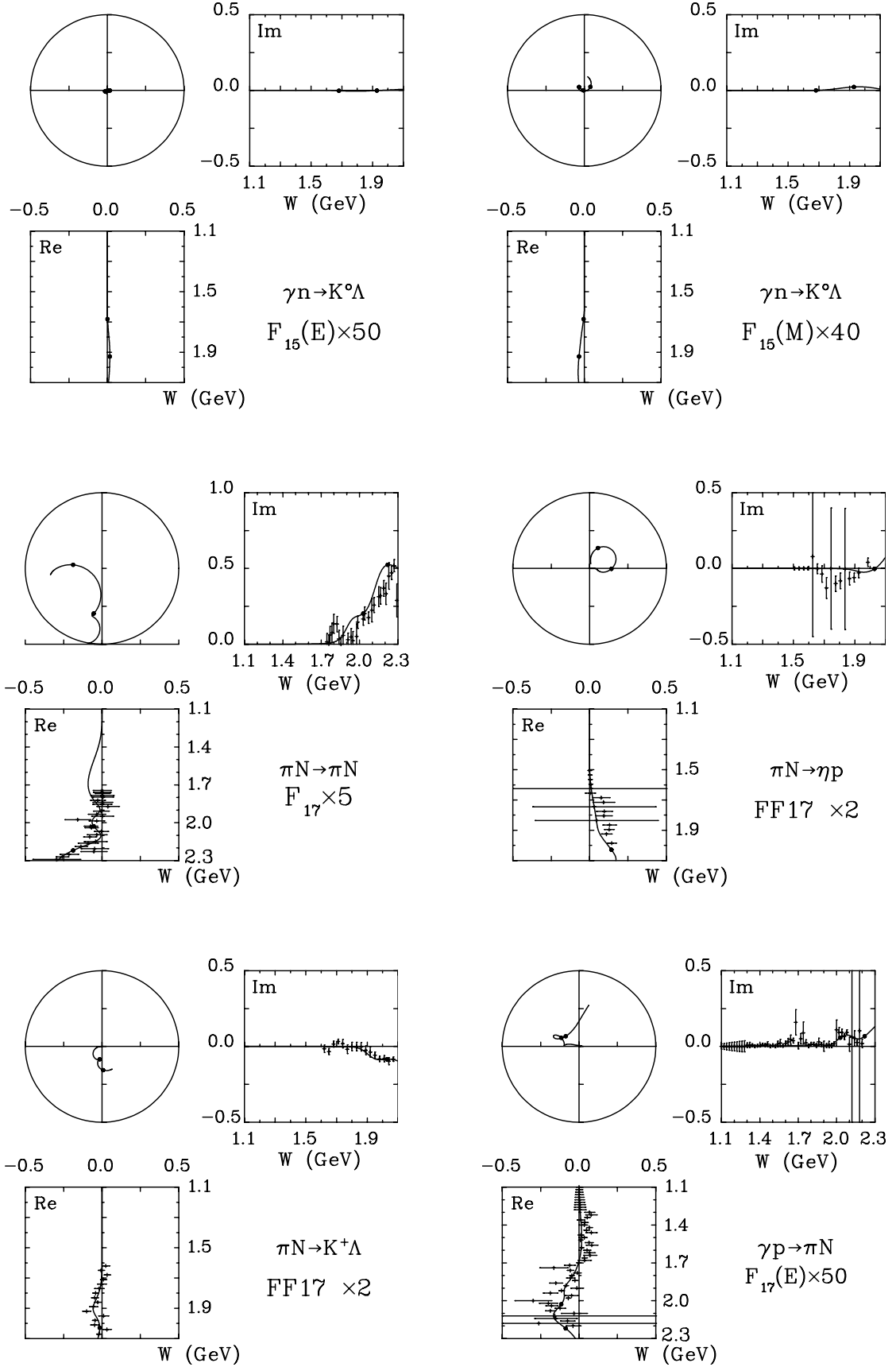
FIG. 13. Argand diagrams for the  $I = 1/2$  amplitudes.

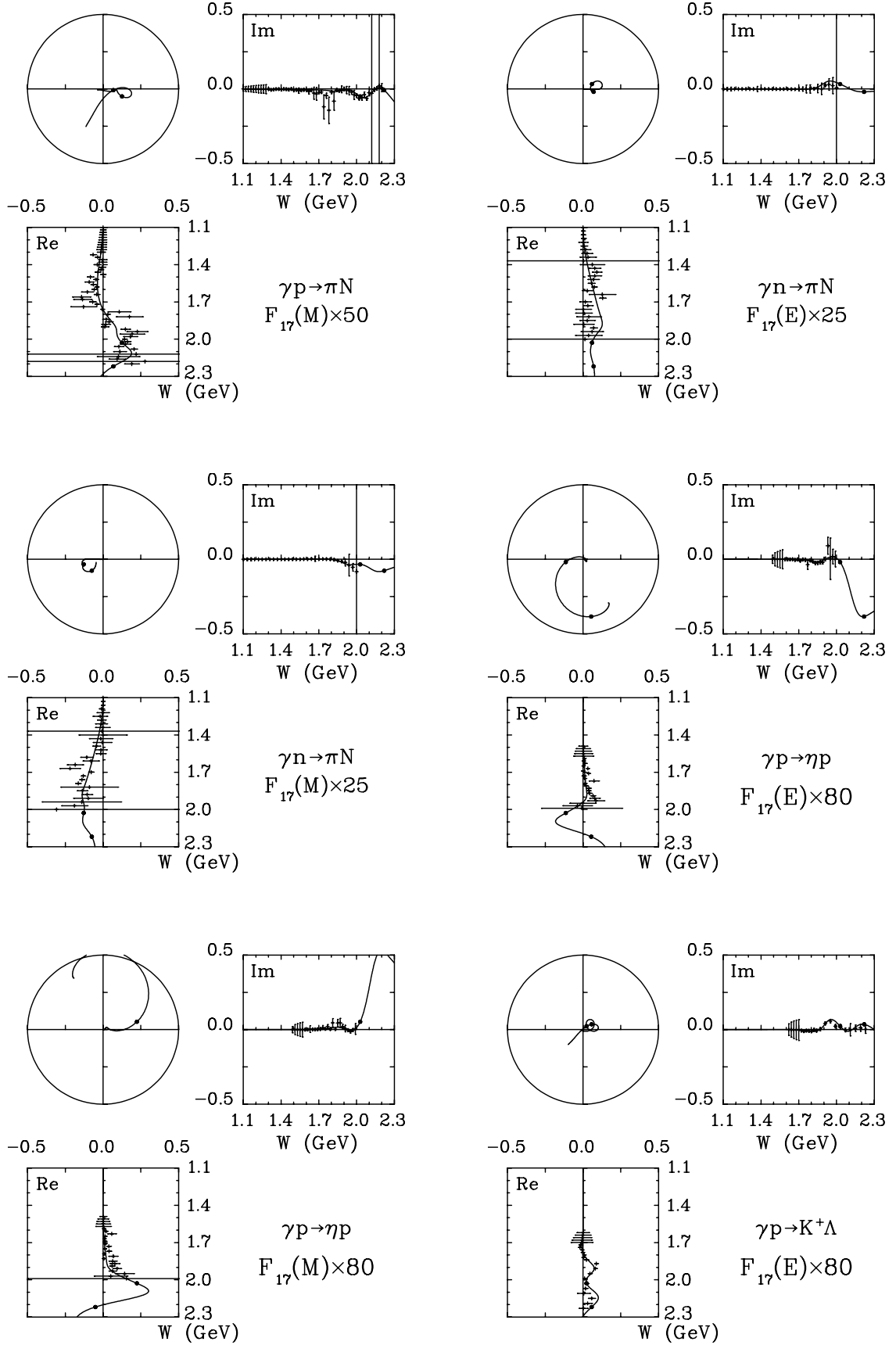
FIG. 14. Argand diagrams for the  $I = 1/2$  amplitudes.

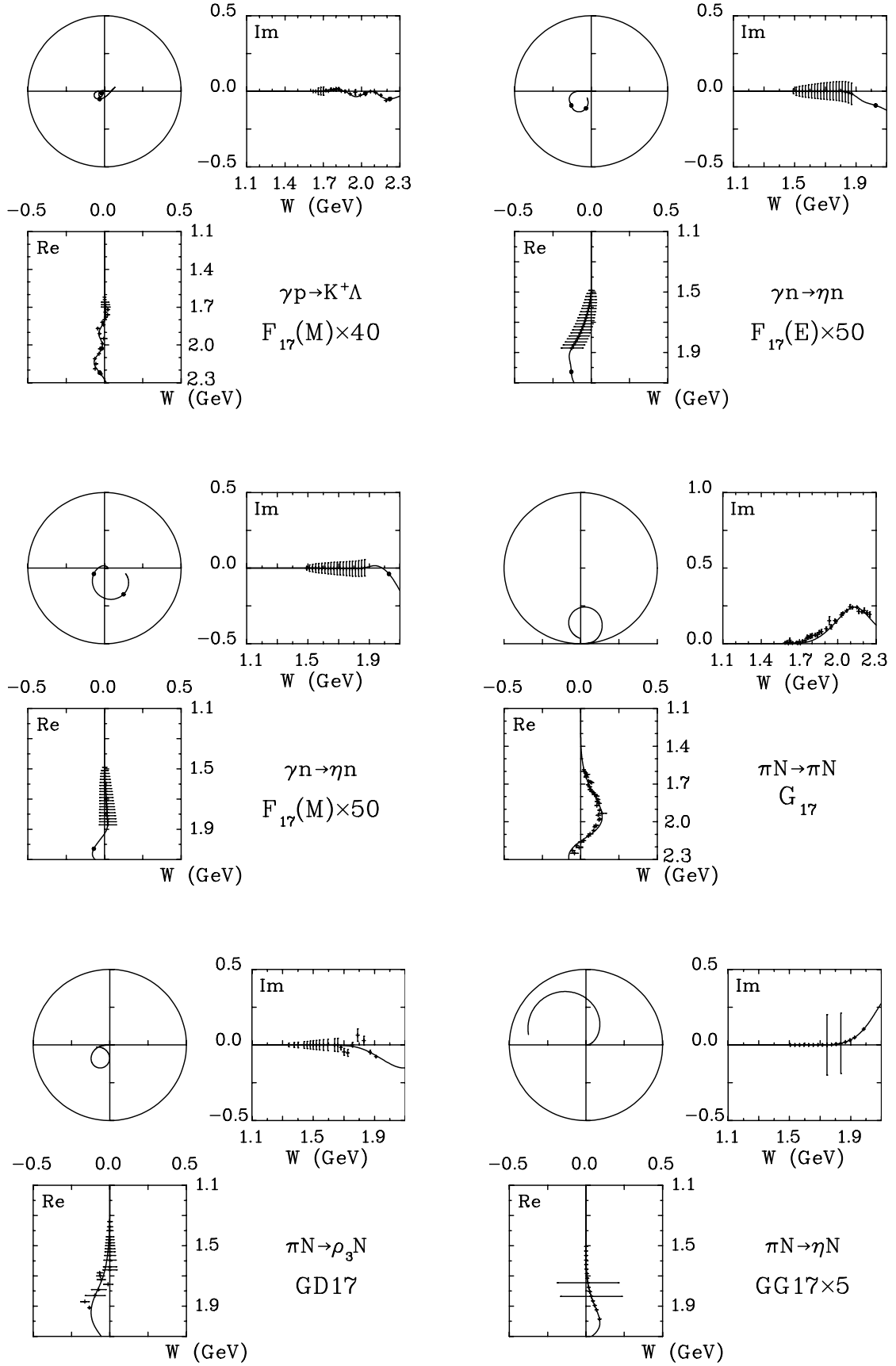


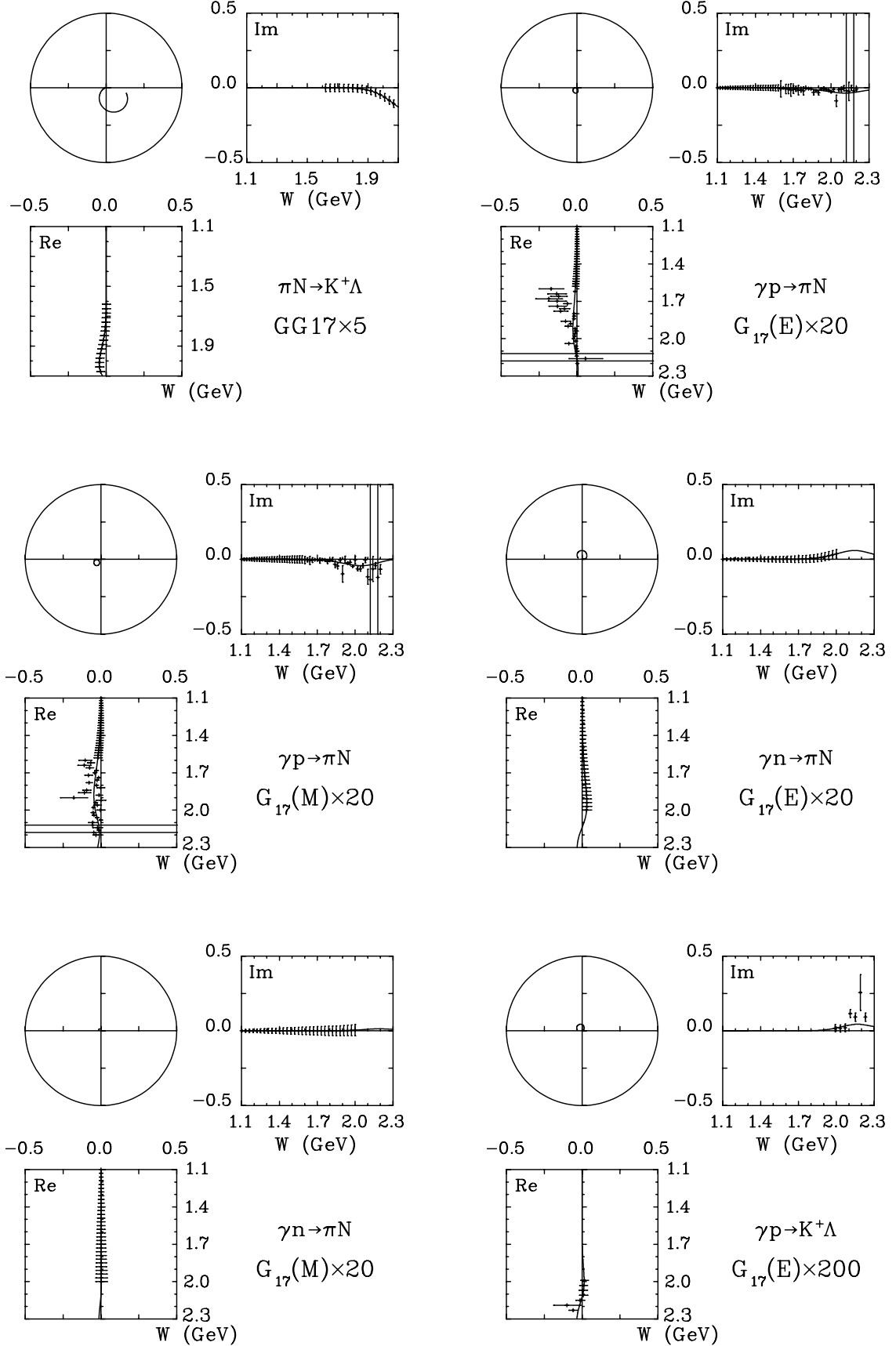
FIG. 15. Argand diagrams for the  $I = 1/2$  amplitudes.

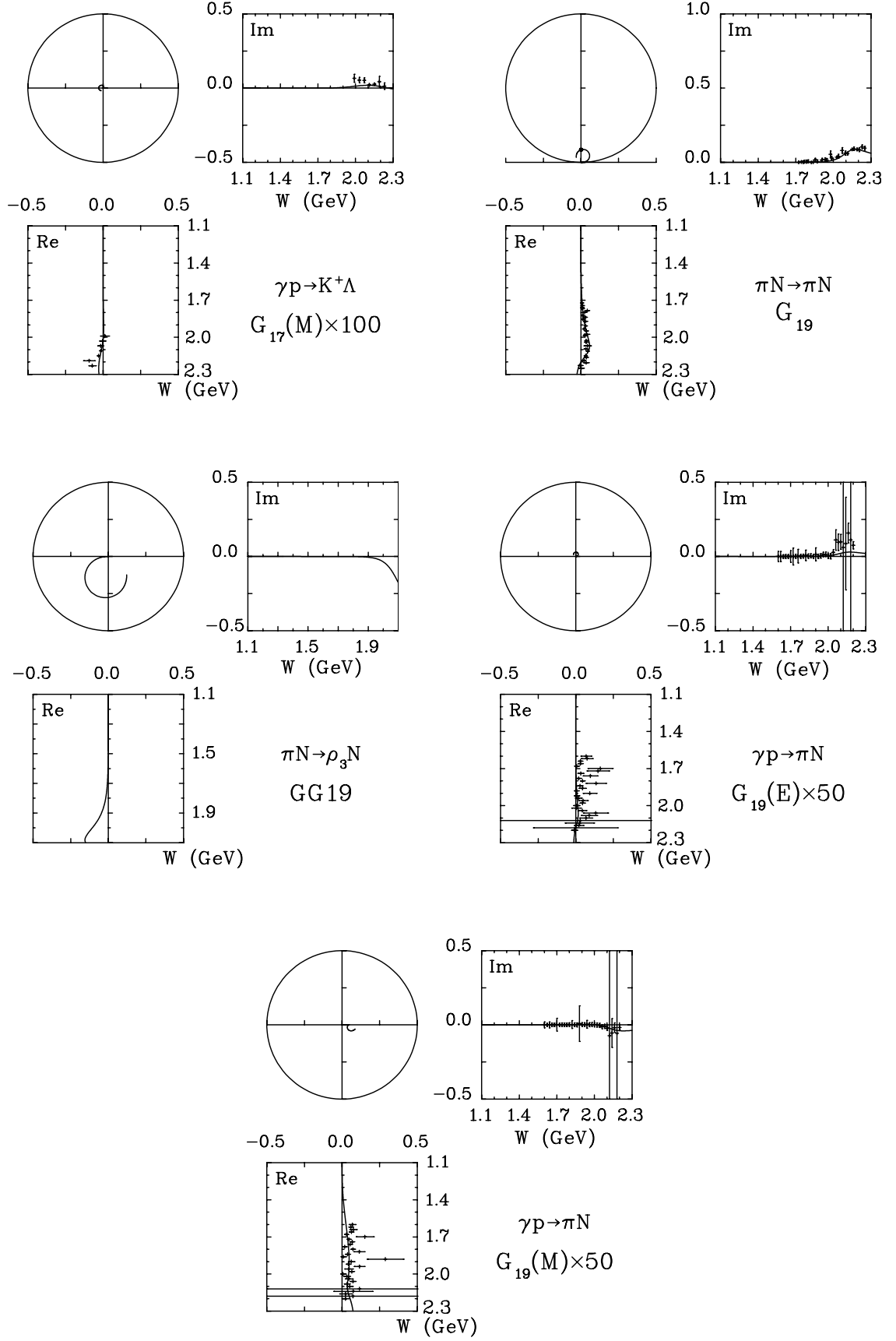
FIG. 16. Argand diagrams for the  $I = 1/2$  amplitudes.

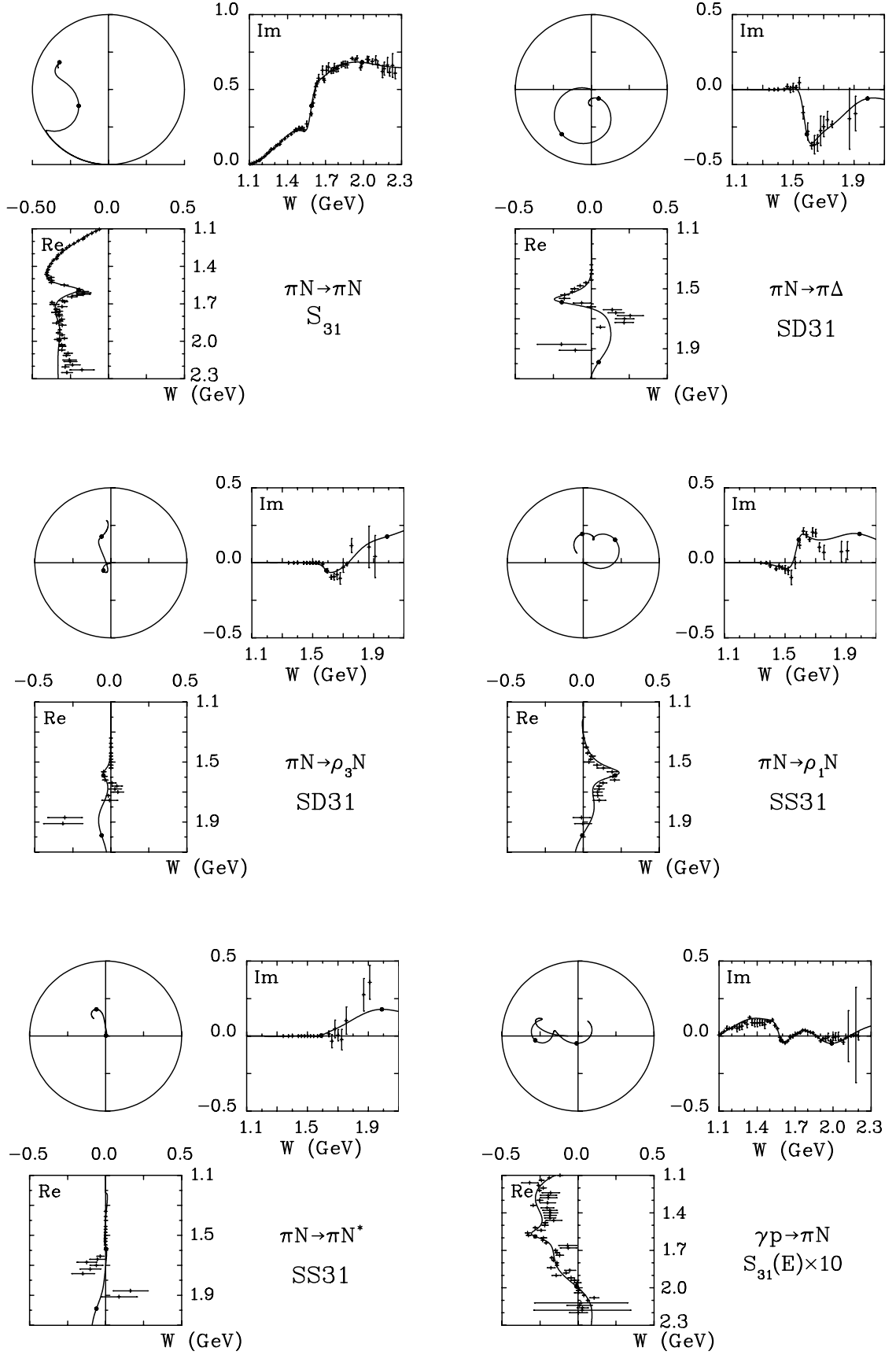
FIG. 17. Argand diagrams for the  $I = 1/2$  amplitudes.

FIG. 18. Argand diagrams for the  $I = 1/2$  amplitudes.

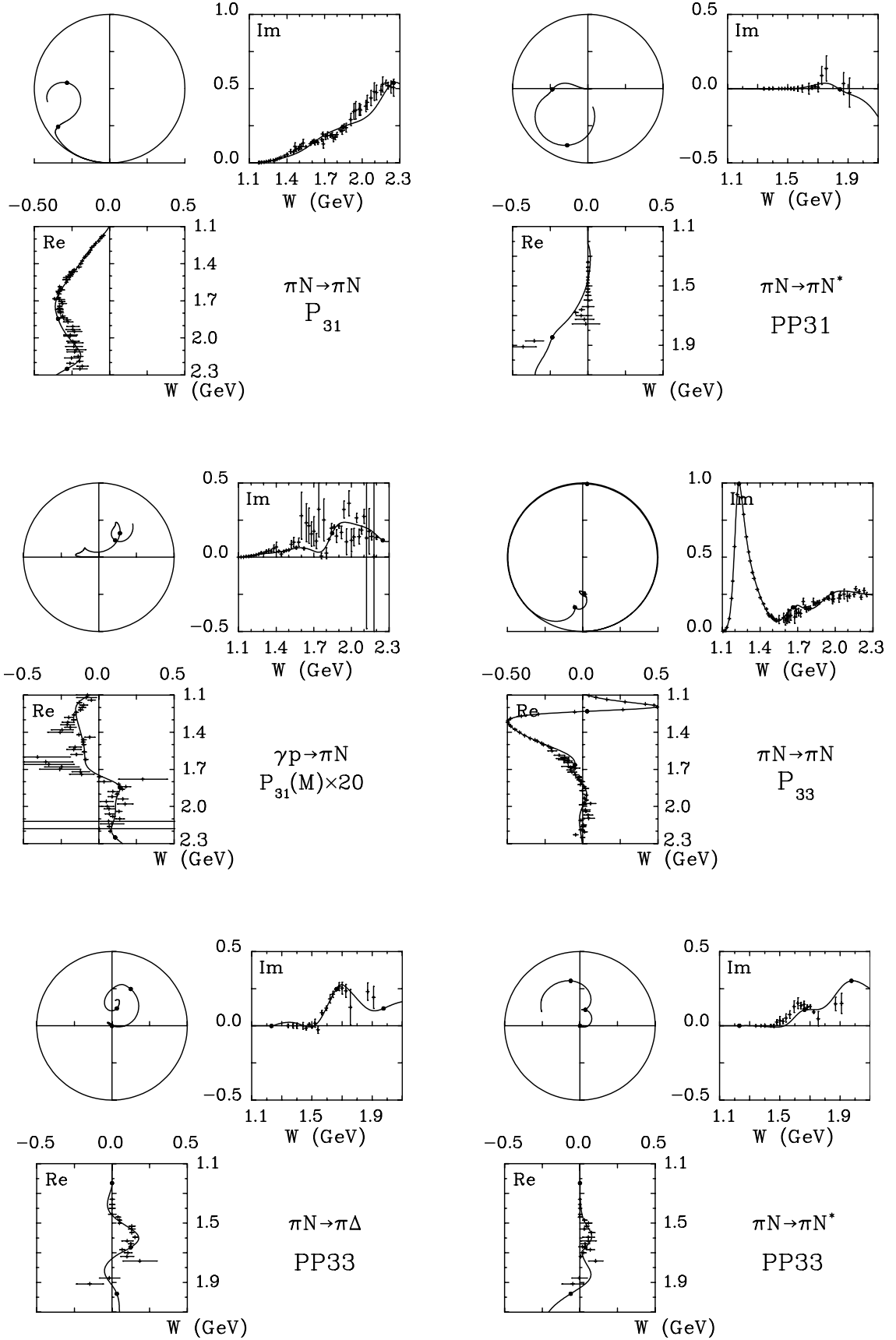
FIG. 19. Argand diagrams for the  $I = 1/2$  amplitudes.

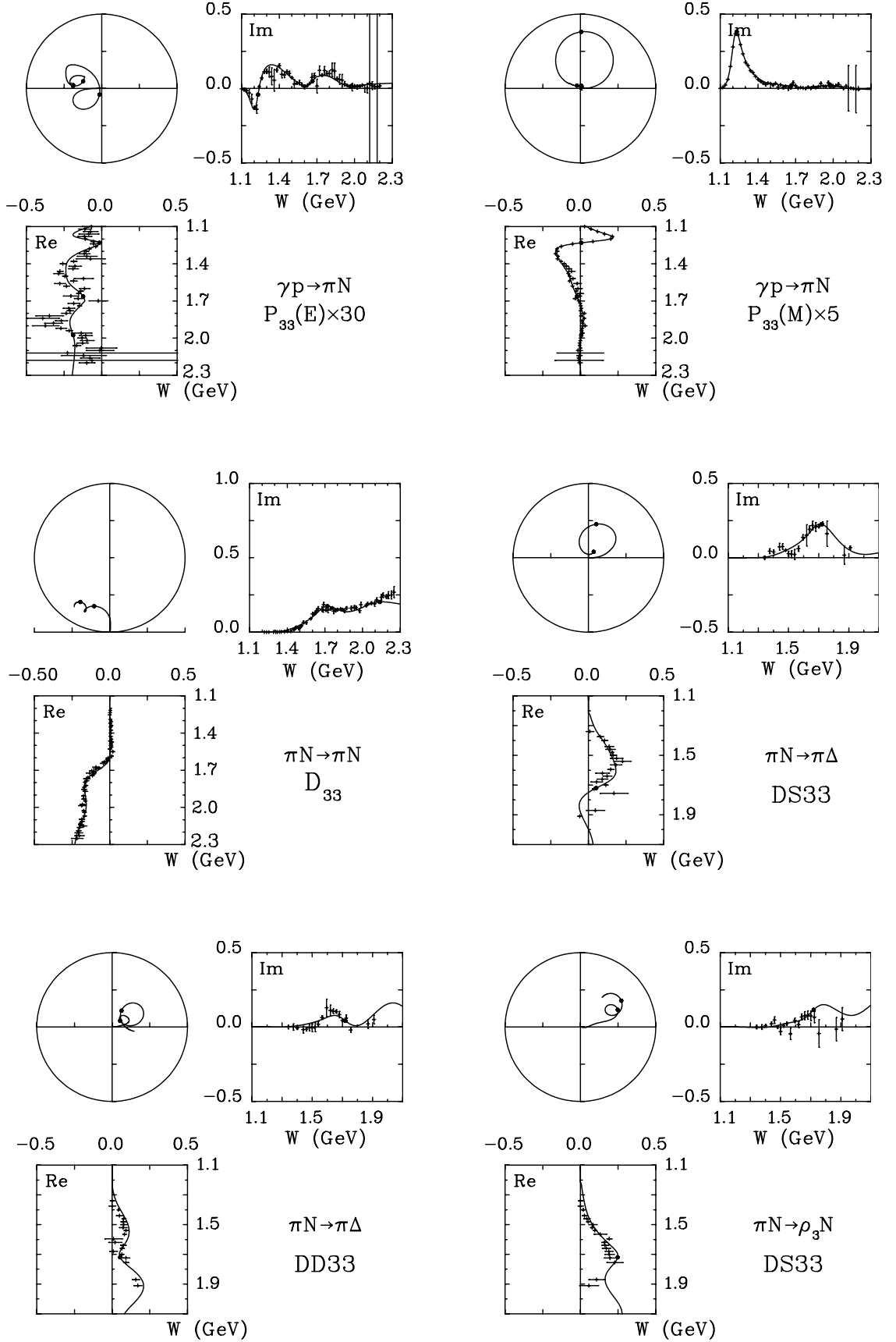
FIG. 20. Argand diagrams for the  $I = 1/2$  amplitudes.

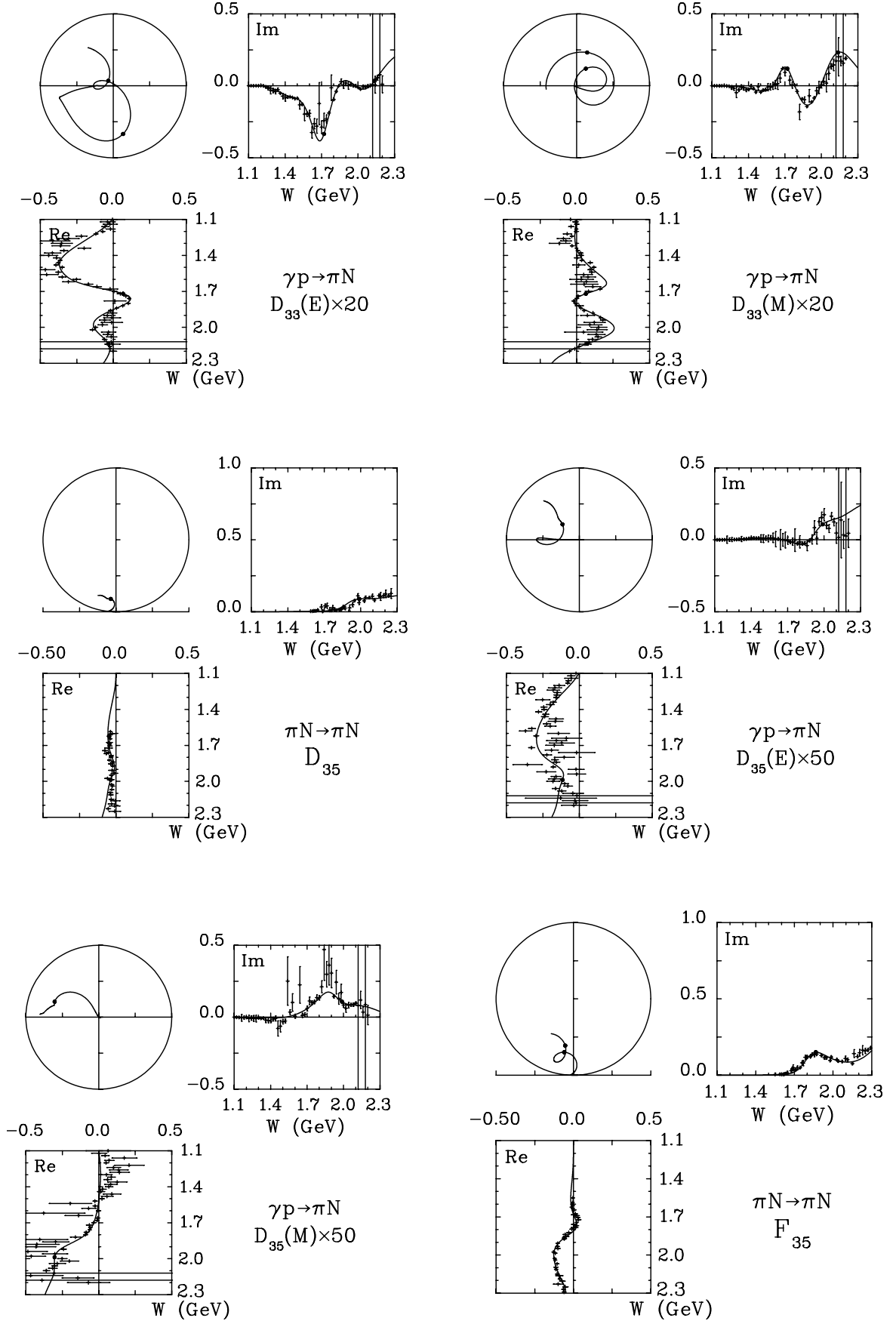

 FIG. 21. Argand diagrams for the  $I = 1/2$  amplitudes.

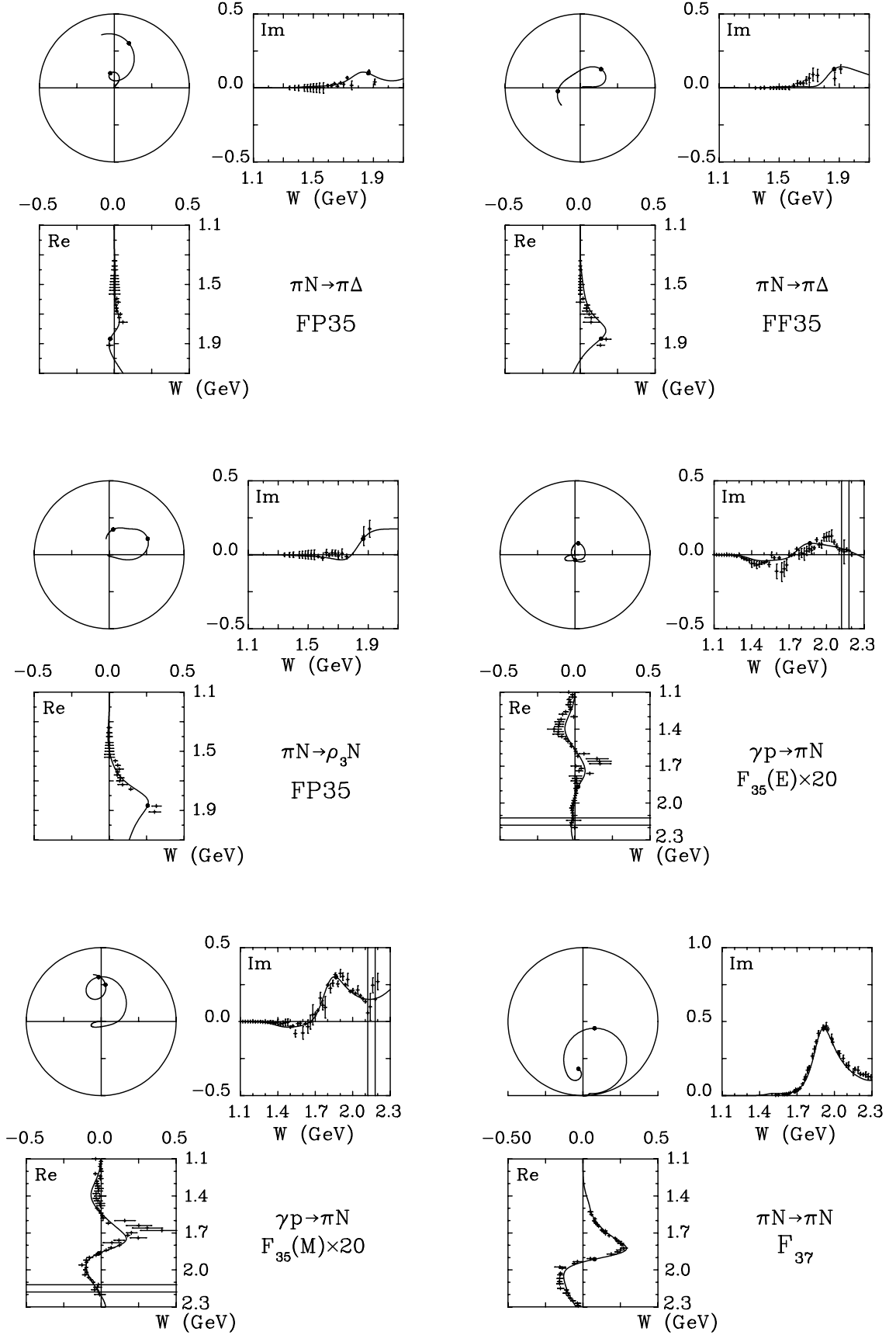
FIG. 22. Argand diagrams for the  $I = 3/2$  amplitudes.

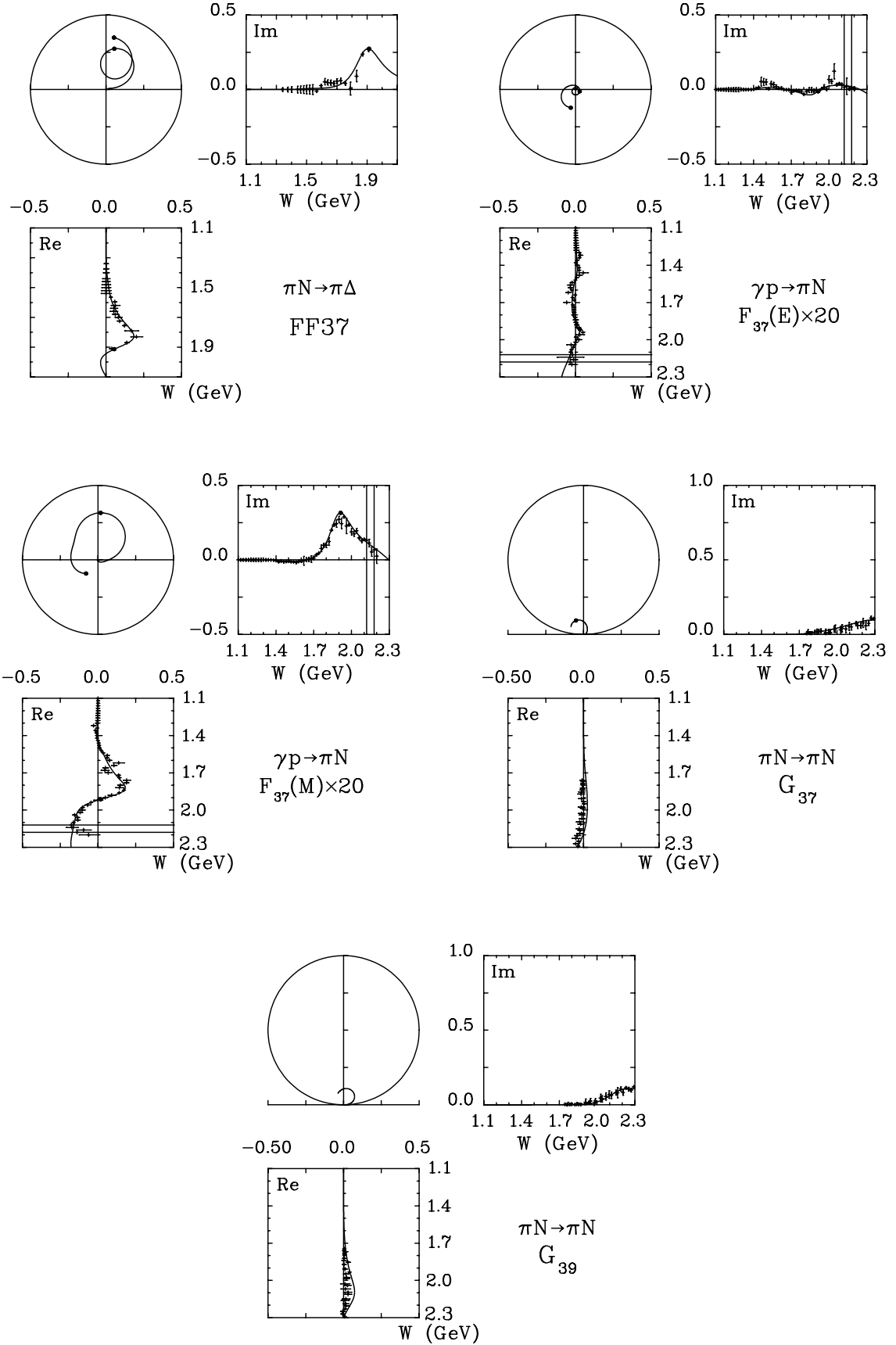


FIG. 23. Argand diagrams for the  $I = 3/2$  amplitudes.

FIG. 24. Argand diagrams for the  $I = 3/2$  amplitudes.

FIG. 25. Argand diagrams for the  $I = 3/2$  amplitudes.

FIG. 26. Argand diagrams for the  $I = 3/2$  amplitudes.

FIG. 27. Argand diagrams for the  $I = 3/2$  amplitudes.